EHMT2 methyltransferase governs cell identity in the lung and is required for KRAS [G12D] tumor development and propagation

Ariel Pribluda[1][*][†], Anneleen Daemen[2][‡], Anthony Nelson Lima[1], Xi Wang[1], Marc Hafner[2], Chungkee Poon[3], Zora Modrusan[4], Anand Kumar Katakam[5], Oded Foreman[5], Jefferey Eastham[5], Jefferey Hung[5], Benjamin Haley[4], Julia T Garcia[6], Erica L Jackson[7][§], Melissa R Junttila[1][*][‡]

[1]Department of Translational Oncology, Genentech, Inc, South San Francisco, United States; [2]Department of Bioinformatics & Computational Biology, Genentech, Inc, South San Francisco, United States; [3]Department of Immunology, Genentech, Inc, South San Francisco, United States; [4]Department of Molecular Biology, Genentech, Inc, South San Francisco, United States; [5]Department of Pathology, Genentech, Inc, South San Francisco, United States; [6]Department of Genetics, Stanford University, Stanford, United States; [7]Department of Discovery Oncology, Genentech, Inc, South San Francisco, United States

*For correspondence:
ariel@surrozen.com (AP);
melissa.junttila@oricpharma.com
(MRJ)

Present address: [†]Surrozen, South San Francisco, United States; [‡]ORIC Pharmaceuticals, South San Francisco, United States; [§]Scorpion Therapeutics, South San Francisco, United States

Abstract Lung development, integrity and repair rely on precise Wnt signaling, which is corrupted in diverse diseases, including cancer. Here, we discover that EHMT2 methyltransferase regulates Wnt signaling in the lung by controlling the transcriptional activity of chromatin-bound β-catenin, through a non-histone substrate in mouse lung. Inhibition of EHMT2 induces transcriptional, morphologic, and molecular changes consistent with alveolar type 2 (AT2) lineage commitment. Mechanistically, EHMT2 activity functions to support regenerative properties of Kras[G12D] tumors and normal AT2 cells—the predominant cell of origin of this cancer. Consequently, EHMT2 inhibition prevents Kras[G12D] lung adenocarcinoma (LUAD) tumor formation and propagation and disrupts normal AT2 cell differentiation. Consistent with these findings, low gene EHMT2 expression in human LUAD correlates with enhanced AT2 gene expression and improved prognosis. These data reveal EHMT2 as a critical regulator of Wnt signaling, implicating Ehmt2 as a potential target in lung cancer and other AT2-mediated lung pathologies.

Editor's evaluation

This is generally a well-designed and carefully conducted study that is likely to be of interest to many both inside and outside of the field of lung tumorigenesis and normal lung development and tissue homeostasis.

Introduction

Lung cancer is the leading cause of cancer mortality in men and women, surpassing combined deaths from colon, prostate and breast cancer (https://www.cancer.org/, 2019). Approximately 40% of non-small cell carcinoma (NSCLC) is of the adenocarcinoma subtype. Genomic alterations of KRAS and

TP53 mutations are the most frequent events within this tumor subtype (*Cancer Genome Atlas Research, 2014*). Considerable evidence indicates that alveolar type 2 (AT2) cells are the predominant cell of origin of lung adenocarcinoma (LUAD) (*Desai et al., 2014*; *Mainardi et al., 2014*; *Sutherland et al., 2014*; *Xu et al., 2012*).

Sustained tumor growth is maintained, in some instances, by a subset of plastic, stem-like cells, referred to as tumor-propagating cells (TPCs) (*Batlle and Clevers, 2017*; *Beck and Blanpain, 2013*). This rare cell subset is less sensitive to therapeutic intervention, and functionally contributes to tumor regrowth following treatment responses (*Beck and Blanpain, 2013*). TPCs are hypothesized to evolve extensively from the tumor-initiating event (*Reya et al., 2001*; *Shackleton et al., 2009*), yet the fidelity to its cell of origin remains undefined. TPCs in LUAD have been previously characterized and were shown to be required for Kras^{G12D} tumor self-renewal (*Zheng et al., 2013*). Moreover, a TPC gene signature correlates with poor prognosis in non-small cell LUAD patients (*Zheng et al., 2013*). While these data implicate a critical function for TPCs in driving tumor progression, it is unknown how these rare cells maintain their stem-like properties.

Wnt signaling is of critical importance in the lung, controlling tissue development, homeostasis and repair processes following lung damage. Wnt signaling is critical in the distal airway to maintain AT2 cell fate and function in the alveolar compartment. A subset of AT2 cells serve as adult tissue stem cells, replenishing themselves, as well as alveolar type 1 (AT1) cells, which are both required to maintain proper alveolar function. Deletion of β-catenin in AT2 cells leads to AT1 cell fate differentiation, demonstrating that β-catenin-mediated Wnt signaling is required for AT2 cell identity (*Frank et al., 2016*; *Nabhan et al., 2018*). Along the same lines, genetic models have also shown the forced expression of a stabilized form of β-catenin engenders aberrant cell fate in mouse lung (*Pacheco-Pinedo et al., 2011*). Together these data indicate that precise Wnt pathway activity is important for alveolar cell function, as well as, cell fate decisions. Furthermore, disruption of Wnt signaling equilibrium can have major consequences in some disease pathologies, including lung cancer (*Nabhan et al., 2018*; *Tammela et al., 2017*; *Zacharias et al., 2018*). What remains unclear is how Wnt signals are intrinsically regulated in cells to maintain or acquire facultative stem-like properties in both homeostatic and disease contexts. Understanding the mechanisms that underlie cell fate decisions may enable therapeutic approaches to enhance or prevent these processes for patient benefit.

In many biological contexts, cellular self-renewal and lineage fate commitment is controlled by epigenetic mechanisms, such as chromatin remodeling (*Easwaran et al., 2014*; *Hemberger et al., 2009*; *Widschwendter et al., 2007*). Recent work identified expression of the EHMT2 lysine methyltransferase (G9a) as a poor prognostic factor in LUAD (*Chen et al., 2010*; *Huang et al., 2017*). Interestingly, EHMT2 activity has been implicated in the regulation of cell identity during development primarily through its epigenetic histone methyltransferase activity (*Chen et al., 2012*; *Epsztejn-Litman et al., 2008*). While EHMT2 methyltransferase activity and its regulation of chromatin is well-described; the non-histone targets of epigenetic regulators are emerging as critical signaling mediators. Here, we investigated how EHMT2 methyltransferase functions to regulate cell fate in distinct cellular contexts relevant for lung tumor development, propagation and AT2 biology. We discover a mechanism of cell intrinsic Wnt signaling control that is governed by EHMT2 activity, establishing EHMT2 as a crucial arbitrator of cell fate gene expression in the lung. By discovering this alternative cell-intrinsic mechanism of governing Wnt signaling in cells, we are able to manipulate cell fate decisions to predictably limit the functionality of these cells to disable tumor propagation, development and AT2 trans-differentiation.

Results

EHMT2 activity is required for *Kras^{G12D};Trp53* (KP) tumorsphere self-renewal

Given the association of EHMT2 expression and poor prognosis in LUAD (*Chen et al., 2010*; *Huang et al., 2017*), we sought to examine the expression and function of EHMT2 in primary murine *Kras^{G12D};Trp53$^{-/-}$* (KP) tumors. Previous work established that KP tumor self-renewal was dependent on a TPC subset. Therefore, by utilizing the previously characterized surface markers CD24, ITGB4, and NOTCH (*Zheng et al., 2013*), we sorted the TPC population and evaluated EHMT2 protein expression. Using two distinct detection methods we observed a consistent and robust increase in EHMT2 protein
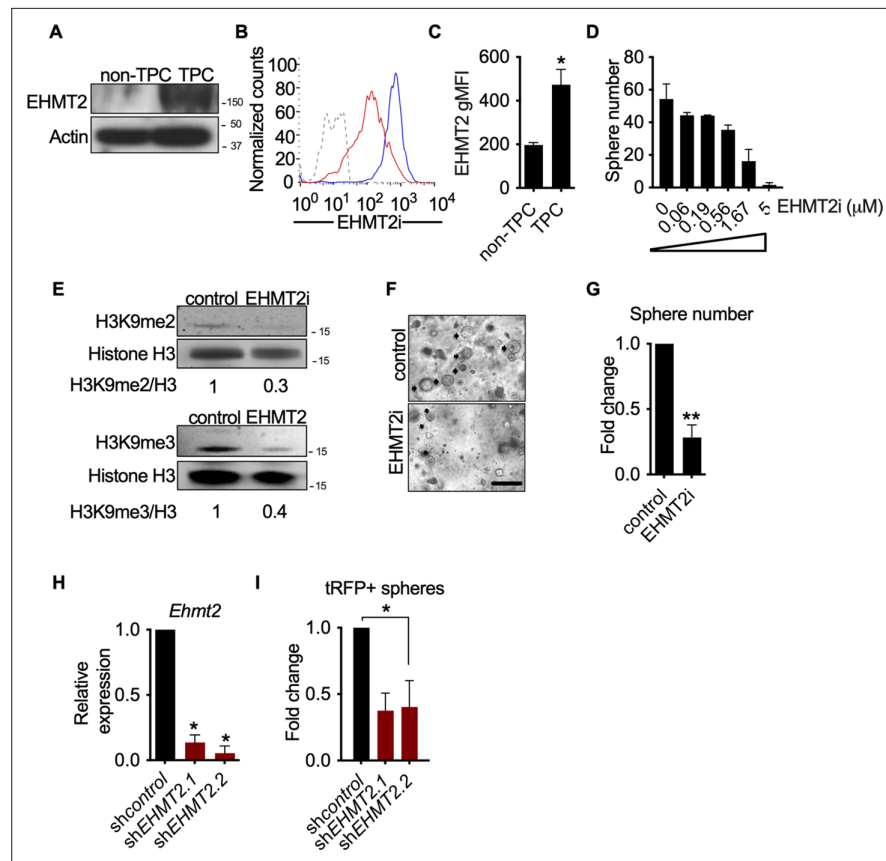
Figure 1. EHMT2 activity is required for $Kras^{G12D};Trp53$ (KP) tumorsphere self-renewal. (**A**) Western blot analysis of EHMT2 in tumor-propagating cell (TPC) and non-TPC. Actin was used as loading control. (**B**) Flow cytometry analysis of EHMT2 in TPC and non-TPC (blue, TPC, red, non-TPC; gray, Isotype). (**C**) Quantification of EHMT2 geometric fluorescence intensity (gMFI) in (**B**) (n=2, mean ± SEM; two-tailed t-test, *p=0.05). (**D**) Tumorsphere formation of KP-derived primary cells seeded with increasing doses of EHMT2 inhibitor (n=2, mean ± SEM, One-way ANOVA with multiple testing, *p<0.005). (**E**) Western blot analysis showing reductions in H3K9me2/3 following EHMT2 inhibitor treatment (EHMT2i, EHMT2 inhibition) histone H3 was used as loading control. Ratio of H3K9me to H3 is depicted at the bottom of the Western blot. (**F**) Representative image of primary tumorspheres following secondary passaging in the absence of either vehicle control or EHMT2 inhibitor (EHMT2i, EHMT2 inhibition. Scale bar 100 μm). (**G**) Quantitation of tumorsphere growth after secondary passaging (n=5; mean ± SEM; two-tailed paired t-test, **p<0.005). (**H**) Relative qRT-PCR of $Ehmt2$ transcripts from primary tumorspheres, expressing either short hairpin RNA (shRNA) control (shControl), or shRNAs against $Ehmt2$ (sh$Ehmt2.$1, sh$Ehmt2.$2), (n=2; mean ± SEM; two-tailed paired t-test, *p<0.05). (**I**) Quantification of turbo RFP (tRFP)-positive tumorspheres following secondary passage of primary tumorspheres expressing control or $Ehmt2$ shRNAs. (sh$Ehmt2.$1, n=2; mean ± SD, sh$Ehmt2.$2, n=3; mean ± SD; two-tailed paired t-test, *p<0.05, shEHMT2.1 p=0.09).

The online version of this article includes the following source data and figure supplement(s) for figure 1:

Source data 1. Western blot for **Figure 1A** showing G9a (EHMT2) in non-TPC vs TPC.

Source data 2. Western blot (right side) for **Figure 1A** showing ACTIN in non-TPC vs TPC.

Figure supplement 1. Schematic overview of tumorsphere assay.

expression (**Figure 1A–C**). Next, we evaluated the requirement of EHMT2 in self-renewal function of TPCs using ex vivo KP-derived organotypic cultures (i.e. tumorspheres), an established surrogate for measuring the in vivo regenerative capability of TPCs (**Zheng et al., 2013**). Pharmacological inhibition of EHMT2, using UNC0642 (**Liu et al., 2013**), resulted in a dose-dependent decrease of primary ex vivo KP-derived tumorsphere formation (**Figure 1D**). Pharmacological inhibition of EHMT2 in established tumorspheres led to a marked reduction in both histone H3 lysine 9 di- and tri-methylation marks (H3K9me2/3), consistent with potent EHMT2 inhibition (**Collins and Cheng, 2010**; **Epsztejn-Litman et al., 2008**; **Shinkai and Tachibana, 2011**; **Figure 1—figure supplement 1**). Both UNC0642
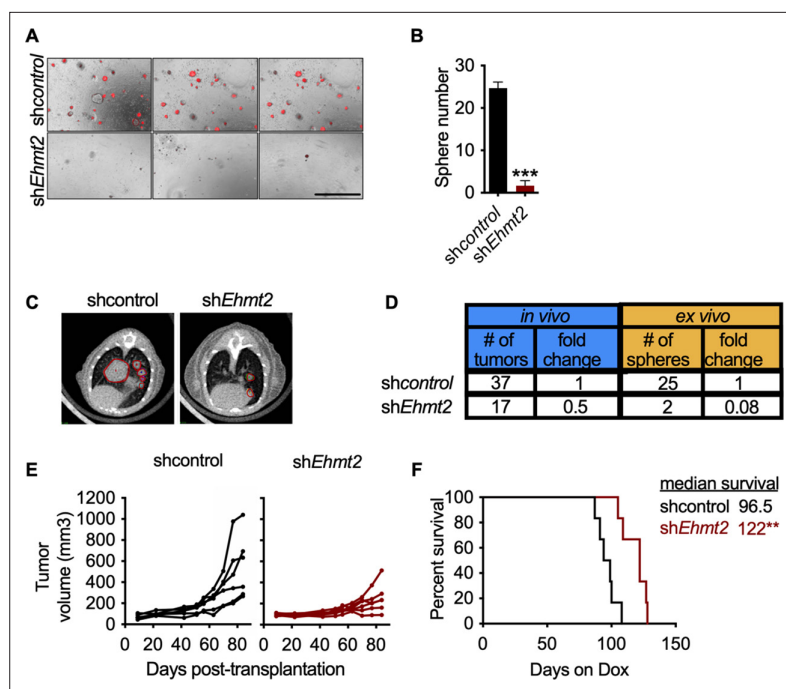
Figure 2. EHMT2 is required for in vivo tumor self-renewal. (**A**) Ex vivo analysis of tumorsphere formation from primary orthotopic transplanted cells, expressing either short hairpin RNA (shRNA) control (sh*control*) or shRNAs against *Ehmt2* (sh*Ehmt2*) (n=3 ± SD) Scale bar 500µM. (**B**) Quantification of tumorsphere formation in panel (**A**), two tailed t-test, ***p<0.0005 (**C**) Representative µ-CT images of shcontrol- or sh*Ehmt2*-expressing tumors (n=6) red circles depicting tumors. (**D**) Table comparing efficiencies of secondary passage in vivo and ex vivo from orthotopically-transplanted primary KP cells, expressing sh*control* (n=6) or sh*Ehmt2* (n=6). (**E**) Overall tumor volume in secondary recipient mice orthotopically transplanted with KP cells from primary recipients, expressing either shRNAs targeting control (sh*control*) or *Ehmt2* (sh*Ehmt2.1*) (n=6) tumor volume at end of study by treatment, Mann-Whitney test, *p<0.05. (**F**) Graph indicates survival of mice depicted in (**E**) (n=6 per group. Geha-Breslow-Wilcoxon test, **p<0.005).

The online version of this article includes the following figure supplement(s) for figure 2:

Figure supplement 1. Analysis of in vivo serial orthotopic transplantation of primary KP cells harboring *Ehmt2* targeting hairpins.

Figure supplement 2. Analysis of terminal tumors from in vivo serial orthotopic transplantation of primary KP cells harboring *Ehmt2* targeting hairpins.

treatment or short hairpin RNA (shRNA)-mediated depletion of *Ehmt2* similarly impaired secondary sphere formation (**Figure 1F–I**), albeit only shEHMT2.2 reached statistical significance, establishing a requirement for EHMT2 activity in TPC self-renewal.

EHMT2 is required for in vivo tumor growth

Previous work has demonstrated that serial re-growth of KP tumors following orthotopic transplantation requires a sustained functional TPC population (**Zheng et al., 2013**). To evaluate the functional necessity of EHMT2 activity on in vivo tumor formation, we evaluated tumor formation following serial transplantation of orthotopically transplanted KP-derived primary cells harboring doxycycline (Dox)-inducible shRNAs. First, hairpin expression was induced in vivo for 13 days by doxycycline administration to mice with established primary lung tumors. Thereafter, shRNA-expressing cells were sorted from primary tumors and assessed for secondary tumorsphere formation ex vivo and tumor formation in vivo (**Figure 2—figure supplement 1A-C**). Sorted sh*Ehmt2*-expressing cells from primary recipients showed a significant decrease in both ex vivo tumorspheres and in vivo secondary tumor formation, establishing a role for EHMT2 in maintaining TPC stemness (**Figure 2A–D**). Continuous monitoring of secondary transplants in vivo revealed a substantial growth impairment in sh *Ehmt2* -expressing tumors, which translated to a significant increase in overall survival (**Figure 2E–F**). Mice harboring

sh*Ehmt2*-expressing tumors eventually succumb to tumor outgrowth; however, analysis of terminal tumors revealed re-expression of *Ehmt2* transcript to a level equivalent to that of control tumors (*Figure 2—figure supplement 2A,B*). This data demonstrates that *Ehmt2* expression is required for TPC-tumor growth. Taken together, these data indicate that EHMT2 activity in TPCs functions to maintain the self-renewal capacity of KP tumors.

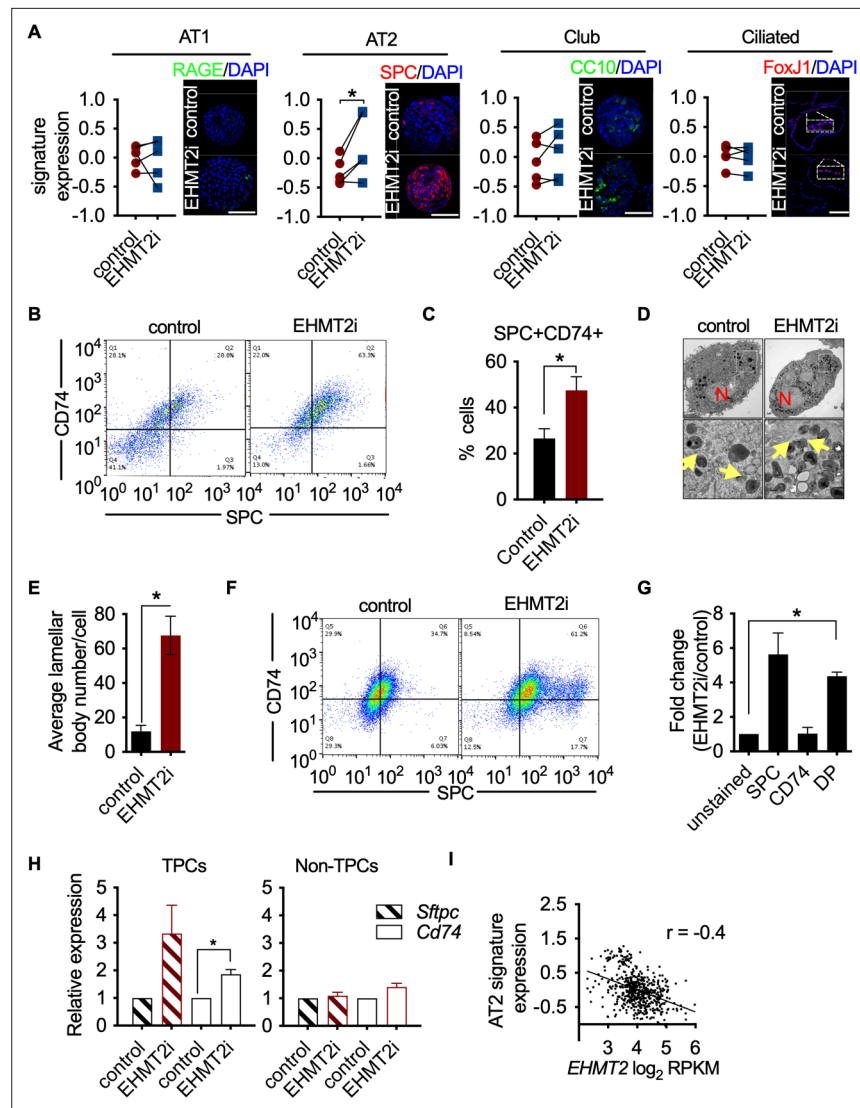## EHMT2 preserves TPC function by preventing AT2 differentiation

To elucidate the mechanistic basis of EHMT2 in maintaining tumor self-renewal, we characterized the phenotypic impact of pharmacological inhibition of EHMT2 in tumorspheres. EHMT2 inhibition resulted in significant reductions in BrdU-labeled cells (fivefold) and expression of cleaved caspase-3 (>10 fold) (*Figure 3—figure supplement 1A-D*). Reduced proliferation and cell death were previously associated with cell differentiation (*Domen and Weissman, 1999*; *Ruijtenberg and van den Heuvel, 2016*), therefore, we further explored cell fate changes as a possible treatment outcome. Since LUAD arises predominantly from the distal alveolar compartment (*Mainardi et al., 2014*; *Sutherland et al., 2014*; *Xu et al., 2012*), we quantified established gene signatures pertaining to distal alveolar cell types from RNA sequencing data derived from EHMT2 i-treated tumorspheres (*Treutlein et al., 2014*). The AT2 gene signature was significantly increased following EHMT2 inhibition, in contrast to other cell lineages (*Figure 3A*). Protein expression of surfactant protein C (SPC), a canonical AT2 marker was also significantly upregulated in EHMT2 -inhibited tumorspheres, likely due to differentiated progenitors (*Figure 3—figure supplement 2*). Concomitant with an increase in SPC+, we observed an increase in CD74, an additional cell surface marker characterizing AT2 cells (*Lee et al., 2013*), showing an increase of the double-positive population (1.8-fold) (*Figure 3B and C*). Moreover, we observed a significant increase in the transcript levels of multiple surfactants in both EHMT2-inhibited and EHMT2-depleted (sh*Ehmt2*) tumorspheres (*Figure 3—figure supplement 3A.B*), indicating increased/enhanced AT2-like cell fate features when EHMT2 activity is impaired. Importantly, this AT2-like conversion was confirmed in *Ehmt2*-depleted tumor cells from secondary passage in vivo (*Figure 3—figure supplement 4*). Furthermore, evidence supporting cell fate transition was observed when transmission electron microscopy (TEM) of EHMT2-inhibited tumorspheres revealed a significant increase in lamellar bodies (*Balis and Conen, 1964*), which are distinct specialized structures responsible for the storage and release of surfactants and serve as a morphometric readout for AT2 cells (*Figure 3D and E*). Together these results demonstrate that EHMT2 inhibition triggers an enhanced/reinforced AT2-like cell state in KP-derived tumorspheres.

As EHMT2 activity is critical for the self-renewal of tumorspheres and its expression is selectively enriched in TPCs, we interrogated whether the observed cell fate changes occur within the TPC fraction. EHMT2 inhibition in primary tumorspheres caused a reduction in TPCs, (*Figure 3—figure supplement 5*), consistent with their reduced stemness. Notably, EHMT2-inhibited TPCs displayed a statistically significant increase (fourfold) in the AT2 surface markers, SPC and CD74, compared to matched controls (*Figure 3F and G*). Consistently, *Sftpc* and *Cd74* transcripts increased exclusively in TPCs (*Figure 3H*). Together, these data indicate that EHMT2 inhibition leads to an induced AT2-like cell state within the TPC subset, thereby reducing their regenerative capacity by a mechanism similar in features to differentiation. To assess whether the relationship between EHMT2 activity and cell state extends to human tumors, we used clinical adenocarcinoma specimens and assessed the association between *EHMT2* transcript and cell lineage gene signatures (*Treutlein et al., 2014*) in a panel of 546 LUADs (*Cancer Genome Atlas Research, 2014*). Consistent with our murine data, *EHMT2* gene expression negatively correlates with the AT2 cell gene signature (*Figure 3—figure supplement 6*), supporting the concept that EHMT2 activity impairs differentiation. Taken together, the data indicate that EHMT2 activity represses an alveolar differentiation program in murine LUAD as a means to preserve stem-like properties that enable tumor self-renewal.

Wnt activation impairs TPC self-renewal and induces AT2 cell lineage marker expression

Previous work indicates that EHMT2 can suppress promiscuous transcription by regulating chromatin structure through the positioning of repressive H3K9 methylation marks in a context-dependent manner (*Chen et al., 2012*; *Kim et al., 2017*; *Zylicz et al., 2018*). We performed an assay for transposase-accessible chromatin using sequencing (ATAC-seq) to characterize chromatin accessibility in EHMT2

Figure 3. EHMT2 preserves TPC function by preventing AT2 differentiation. (**A**) Graphs show enrichment analyses of distinct alveolar cell-lineage gene signatures in transcriptomes generated from KP-derived primary tumorspheres following EHMT2 inhibition (EHMT2i) vs vehicle control (control) (n=4; mean Z-score ± SEM, two-tailed paired t-test, *p<0.05), each paired with immunofluorescence (IF) micrographs of representative canonical marker from their respective cell lineage. Scale bar 100μM (See Figure (S3E) for quantitation of IF). (**B**) Representative flow cytometry of cells derived from primary tumorspheres treated with either vehicle control (control) or EHMT2 inhibitor (EHMT2i) for 5 days and immuno-stained for alveolar type 2 (AT2) markers surfactant protein C (SPC) and CD74. (**C**) Quantification of the SPC-CD74 double positive (DP) population depicted in (**B**). (n=4; mean ± SEM, two-tailed paired t-test, *p<0.05). (**D**) Representative transmission electron microscopy (TEM) image of cells extracted from primary tumorspheres, treated as in (**B**). (Upper panel, scale bar 2 μm; lower panel, respective insets in the upper panel, scale bar 0.5 μm). (N, nucleus; yellow arrows, lamellar bodies). (**E**) Quantification of TEM in (**D**) (n=2; mean ± SEM, two-tailed paired t-test, *p<0.05). (**F**) Representative flow cytometry of tumor-propagating cells (TPCs) sorted after EHMT2 inhibitor (EHMT2i)- or vehicle control-treatment of primary tumorspheres and immuno-stained for AT2 markers SPC and CD74. (**G**) Quantification of (**F**), showing fold-change in EHMT2i/control ratio of AT2 markers SPC and CD74 (n=2; mean ± SEM, One-way ANOVA with Tukey's multiple comparison test, **p<0.005). (**H**) Relative expression of *Sftpc* and *Cd74* transcripts in EHMT2i vs control; TPC and non-TPC, respectively. (n=3; mean ± SEM, two-tailed paired t-test, *p<0.05). (**I**) Spearman's rank correlation analysis between orthogonal human AT2 gene signatures and *EHMT2* transcript in 546 human lung adenocarcinomas (LUAD). (n=546, linear regression analysis, ***p<0.0001, *r*=−0.4).

The online version of this article includes the following figure supplement(s) for figure 3:

Figure 3 continued on next page

Figure 3 continued

Figure supplement 1. EHMt2 inhibition reduces apoptosis and proliferation in tumorspheres.

Figure supplement 2. Quantification of immunostaining in control and EHMT2i-treated tumorspheres (RAGE: control, n=28; EHMT2i, n=21).

Figure supplement 3. Induction of surfactants following EHMT2 depletion and pharmacologic inhibition.

Figure supplement 4. Relative expression of alveolar type 2 (AT2) markers in tRFP-sorted tumor cells derived from primary recipients expressing either shcontrol or sh*Ehmt2* (n=3; mean ± SEM; *Sftpc, Slc34a2,* Lamp3, Cd74; two-tailed paired t-test *p<0.05).

Figure supplement 5. Quantification of tumor-propagating cell (TPC) fraction following EHMT2i vs control (n=19; mean ± SEM; two-tailed paired t-test *p<0.05).

Figure supplement 6. Spearman's rank correlation analysis between orthogonal human alveolar gene signatures and *EHMT2* transcript in 546 human lung adenocarcinomas (LUAD) (n=546, linear regression analysis p<0.0001).

inhibitor-treated, tumorsphere-derived TPCs. Surprisingly, very limited changes in chromatin accessibility were observed in TPCs upon EHMT2 inhibition (*Figure 4—figure supplement 1A,B*), indicating that EHMT2 inhibition does not induce widespread chromatin remodeling: 11 promoter and 320 non-promoter sites became more accessible following EHMT2 inhibition, whereas 3 promoter and 54 non-promoter sites were less accessible (FDR <0.05, fold-change >1.5). The promoter sites were not disproportionately enriched for any pathway, and could not account for the EHMT2-induced phenotype.

In the absence of EHMT2 i-induced chromatin accessibility changes, we investigated signaling pathways that influence alveolar cell fate decisions in TPCs. A subset of AT2 cells in normal lung act as tissue stem cells, and Wnt signaling is critical for the maintenance of their stem cell identity (*Nabhan et al., 2018*; *Zacharias et al., 2018*). We reasoned that EHMT2 could regulate Wnt signaling as a means to maintain stemness and prevent differentiation in TPCs. Consistent with this line of reasoning, EHMT2 inhibition resulted in a statistically significant increase in *Axin2* expression only within the TPC subset (*Figure 4A*), implicating a functional link between EHMT2 activity and Wnt signaling.

Since EHMT2 inhibition led to *Axin2* upregulation whilst impairing TPC self-renewal and inducing an AT2-like cell fate, we assessed whether Wnt activation alone was sufficient to achieve these outcomes. Indeed, pharmacological activation of Wnt signaling using two doses of the GSK3β inhibitor CHIR99021 (*Figure 4B* and *Figure 4C*) impaired TPC stemness as illustrated by reduced tumorsphere self-renewal, consistent with EHMT2 inhibition (*Figure 4B–F*). Moreover, corresponding Wnt pathway activation and transcriptional activation of AT2 marker genes was observed at secondary passage (*Figure 4E*), with a concordant dose-dependent increase in SPC surface expression (*Figure 4F*). To better understand the link between Wnt pathway activation and selective increase of AT2 cell lineage gene expression, we performed an unbiased analysis of transcription factor binding motifs within the promoters of cell lineage signature genes (*Treutlein et al., 2014*). We found that the *Tcf4* motif ranked eighth among 264 tested motifs for AT2 genes, while ranking much lower for other cell lineages, supporting the concept that AT2 cell fate is directly linked to a Wnt-driven signaling process (*Figure 4—figure supplement 2*). Moreover, 4 out of 7 *Tcf4*-containing AT2 genes are significantly induced in TPCs upon EHMT2 inhibition (*Figure 4—figure supplement 3*), further supporting the concept that the EHMT2 -inhibitor phenotype is Wnt-mediated. Notably, the *Tcf4*-containing AT2 genes that are induced upon EHMT2 inhibition display accessible chromatin configurations at their promoters irrespective of treatment (*Figure 4—figure supplement 4*), suggesting that these genes are poised to respond to Wnt-mediated signals and therefore would not require chromatin accessibility changes to enable gene expression (*Zacharias et al., 2018*).

EHMT2 restrains Tcf4 gene transcription by repressing chromatin bound β-catenin through RUVBL2

Given the convincing link between inhibition of EHMT2 activity and Wnt-mediated AT2 gene expression, we sought to elucidate the mechanistic basis for Tcf4-mediated gene transcription. Since we observed only a limited change in chromatin accessibility in response to EHMT2 inhibition, we reasoned that a non-histone substrate may be controlling this process. Previous reports have shown that EHMT2 -dependent methylation of the non-histone substrate RUVBL2 (REPTIN, TIP48, and
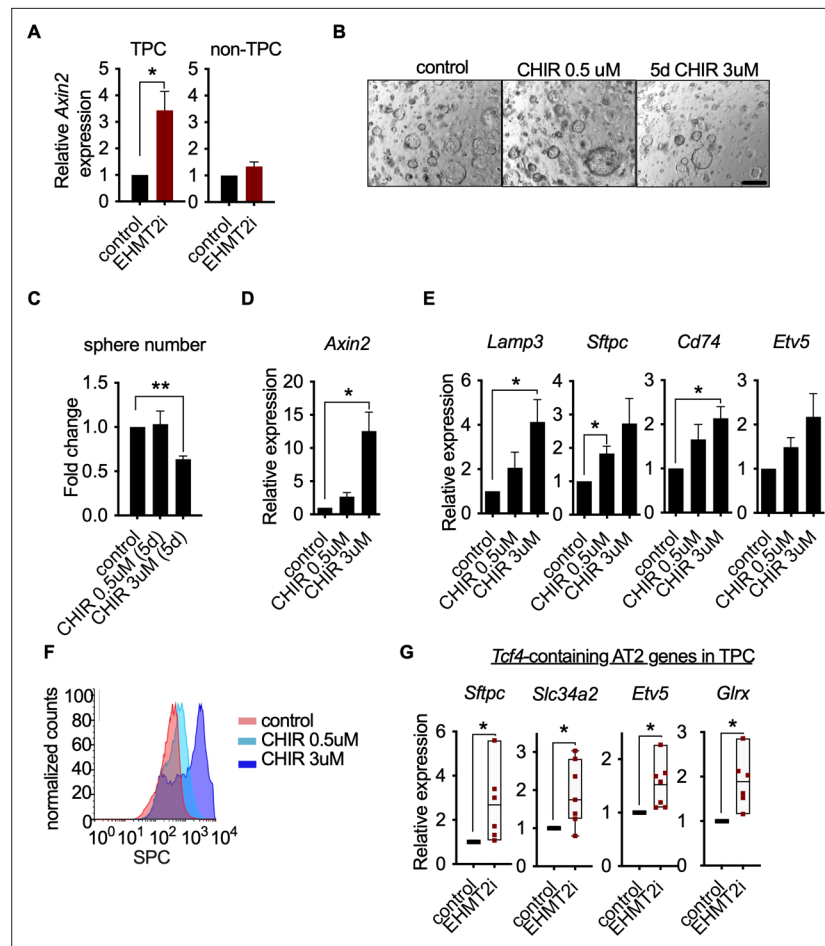
Figure 4. Wnt activation impairs TPC self-renewal and induces AT2 cell lineage marker expression. (**A**) Relative expression of *Axin2* transcripts in tumor-propagating cells (TPCs) and non-TPC following EHMT2 inhibition (EHMT2i) vs vehicle control (control) (n=4 mean± SEM; two-tailed paired t-test, *p<0.05). (**B**) Representative micrographs of primary tumorspheres passaged to single cells following 5 days of the GSK3b inhibitor, CHIR (5 days CHIR) at indicated doses vs vehicle control (control) and assessed for secondary sphere formation (scale bar 100 μm). (**C**) Quantification of sphere formation experiments as represented in (**b**) (n=4 mean ± SEM; two-tailed paired t-test, **p<0.005). (**D**) Relative expression of *Axin2* transcripts in primary tumorspheres (n=5 mean ± SEM, two-tailed paired t-test, *p<0.05). (**E**) Relative expression of alveolar type 2 (AT2) markers in tumorspheres (n=5 mean ± SEM, two-tailed paired t-test, *p<0.05). (**F**) Flow cytometry for surfactant protein C (SPC) in primary tumorspheres, treated with two doses of GSK3β inhibitor (CHIR) for 5 days vs vehicle control (control). (**G**) Relative expression of TCF4-containing AT2 markers in TPCs, treated with EHMT2i vs control (n=6, mean ± SEM, two-tailed paired t-test, *p<0.05).

The online version of this article includes the following figure supplement(s) for figure 4:

Figure supplement 1. EHMT2 inhibition does not induce broad changes in chromatin accessibility.

Figure supplement 2. Unbiased enrichment analysis of transcription factor (TF) binding motifs, revealing enrichment of *Tcf4* motifs in promoter regions of distal alveolar cell-lineage gene signatures vs background, depicted in red and gray color bars, respectively.

Figure supplement 3. Relative expression of TCF4-containing alveolar type 2 (AT2) markers in tumor-propagating cells (TPCs), treated with EHMT2i vs control (n=6, mean ± SEM,).

Figure supplement 4. Integrated genome viewer tracks of transposase-accessible chromatin using sequencing (ATAC-seq) generated from tumor-propagating cells (TPCs).

TIP49b) can repress HIF1α-mediated transcription (*Lee et al., 2010*). RUVBL2 has also been shown to antagonize β-catenin activity (*Bauer et al., 2000*; *Mao and Houry, 2017*). We reasoned that the non-histone substrate, RUVBL2, might function to repress β-catenin activity through a EHMT2 -mediated mechanism. First, we confirmed the RUVBL2 and β-catenin interaction in a human NSCLC cell line (*Figure 5A and B*). Immunoprecipitation of RUVBL2 showed its ability to interact with β-catenin and HIF1-α proteins in hypoxic and normoxic conditions (*Figure 5A*), consistent with previously reported results (*Lee et al., 2010*). Reciprocally, immunoprecipitation of β-catenin showed an interaction with RUVBL2. However, the RUVBL2-β-catenin interaction was reduced exclusively in the EHMT2 -inhibited context (*Figure 5B*), indicating that the RUVBL2-β-catenin interaction requires EHMT2 activity, analogous to that of the RUVBL2-HIF-1α (*Lee et al., 2010*). To better visualize the impact of EHMT2 inhibition on the RUVBL2-β-catenin interaction with the relevant TPC subset, we performed proximity ligation assay (PLA). Indeed, PLA confirmed the RUVBL2-β-catenin interaction in TPCs and demonstrated a significant loss of signal in the presence of EHMT2 I, providing additional support for the requirement of EHMT2 activity to maintain the RUVBL2-β-catenin interaction (*Figure 5C and D*).

In order to gain spatial insight into how EHMT2 inhibition impacts the relationship between EHMT2, RUVBL2, β-catenin and chromatin, we performed subcellular fractionation of tumorspheres. While EHMT2 inhibition showed loss of both EHMT2 and RUVBL2 proteins from the chromatin fraction, equal amounts of β-catenin remain chromatin-bound (*Figure 5E*). The sustained levels of chromatin-bound β-catenin following EHMT2 inhibition, suggests a critical role for EHMT2 -mediated RUVBL2 regulation that occurs at the chromatin (*Figure 5E*). Notably, the cytoplasmic fraction of controls confirms the presence of both β-catenin and RUVBL2, consistent with the cytoplasmic signal observed in the TPC PLA control (*Figure 5C–E*). Given that we established that RUVBL2 interacts with β-catenin and RUVBL2 abundance is reduced in the chromatin fraction when EHMT2 activity is inhibited, we tested whether RUVBL2 chromatin occupancy is changed specifically on *Tcf4*-containing AT2 genes in TPCs. We observed over 90% reduction in RUVBL2 promoter occupancy within *Tcf4* elements of AT2 genes *Slc34a2* and *Etv5* (*Figure 5F and G*). Taken together these results indicate that EHMT2 directly controls *Tcf4*-containing AT2 gene expression through RUVBL2-mediated repression of β-catenin transcription.

EHMT2 controls Wnt signaling and differentiation within AT2 cells

We next explored whether EHMT2 functions similarly to regulate β-catenin activity in normal AT2 cells. Pharmacological inhibition of EHMT2 in vivo for 6 days demonstrated a robust induction of Axin2 protein expression in primary distal alveolar cells using flow cytometry (*Figure 6—figure supplement 1A,B*). To assess the impact of EHMT2 inhibitor-mediated Wnt induction on AT2 cell fate, we derived primary AT2 cells from adult murine lung and determined the ability of AT2 progenitors to form alveospheres. Ex vivo culturing of primary AT2 cells leads to the formation of alveospheres with cells resembling both AT2 and AT1 cell fates (*Barkauskas et al., 2013*; *Desai et al., 2014*). In contrast to KP tumorspheres, inhibition of EHMT2 activity did not impair ex vivo alveosphere formation; however, the resulting spheres were significantly smaller relative to controls (*Figure 6B*). During alveosphere formation and expansion, emerging cells express transcriptional and surface markers consistent with an AT2 to AT1 cell differentiation (*Barkauskas et al., 2013*; *Zacharias et al., 2018*). By analyzing expression of surface markers indicative of these fates (*Desai et al., 2014*), we observed that EHMT2 inhibition significantly reduced the proportion of AT1 cells (SPC-PDPN+) from 67.2 to 24.4% (*Figure 6—figure supplement 2*). Interestingly, while the proportion of AT2 cells (SPC +PDPN-) remained unchanged, we observed a marked increase in double positive cells (SPC +PDPN +) from 15 to 62%. Together these data indicate that EHMT2 is required for differentiation of the AT2 progenitor pool and for complete and proper AT1 differentiation. Consistent with our previous results in TPCs, EHMT2 inhibition resulted in enhanced Wnt signaling, reflected by increased *Axin2* expression, as well as *Lgr4* and *Lgr5*, two prominent Wnt signaling pathway components (*de Lau et al., 2011*; *Figure 6D*). The observed increase in *Tcf4*-containing AT2 marker gene expression supports increased Wnt-mediated activity in primary AT2 cells as in the TPC context (*Figure 6E*). In contrast to the TPC subset, we observed significant changes in the proportion of AT1 cells, consistent with the reduced plasticity observed in AT2 cells. These data demonstrate that EHMT2-mediated regulation of Wnt signaling and cell fate is also observable in untransformed, primary AT2 cells. To test whether EHMT2 loss is similarly required for the differentiation of AT2 cells in vivo, we deleted EHMT2 in the alveolar compartment
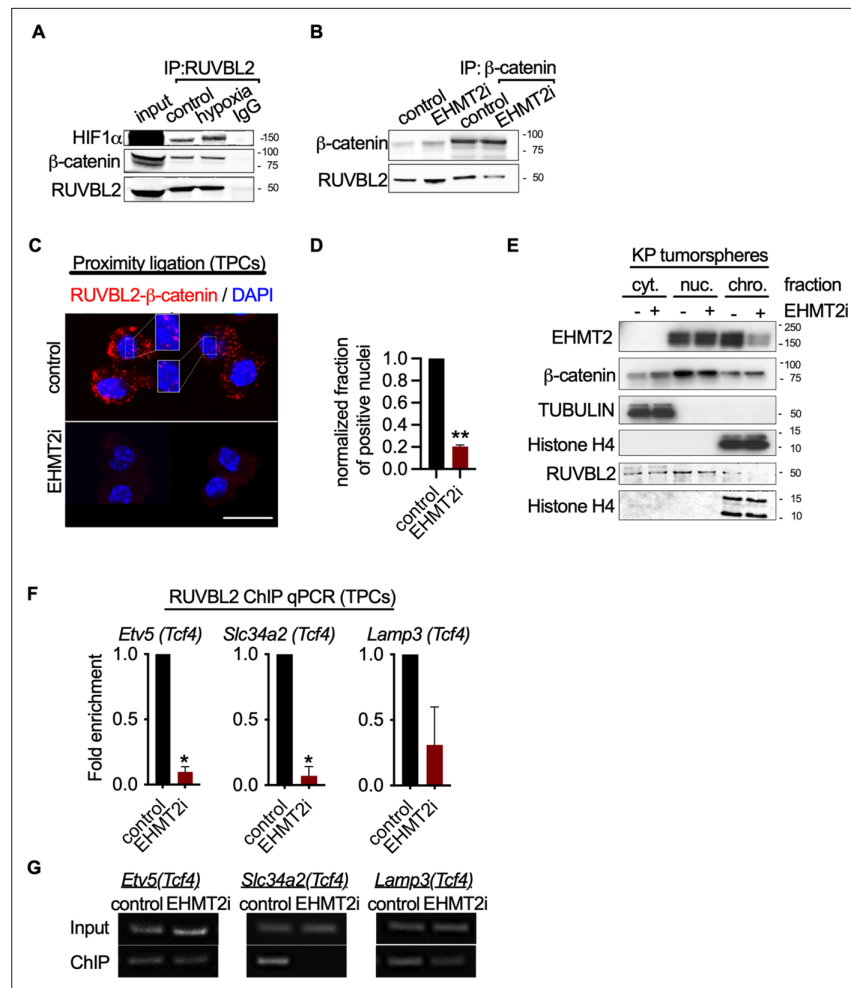
Figure 5. EHMT2 restrains Tcf4-mediated gene transcription by repressing chromatin bound β-catenin through RUVBL2. (**A**) Western blot demonstrating expression of HIF1-α and β-catenin in A549 lysates immunoprecipitated with RUVBL2 antibody. Cells were cultured under hypoxic conditions (1% O_2) vs control (ambient O_2). (**B**) Western blot demonstrating co-immunoprecipitation of RUVBL2 in A549 lysates co-immunoprecipitated with β-catenin antibody. Cells were treated with EHMT2 inhibitor vs control. (**C**) Proximity ligation assay in EHMT2i-treated vs vehicle-treated tumor-propagating cells (TPCs) (red, RUVBL2-β-catenin proximity ligation; blue, DAPI counterstain). Insets show a magnification of the red signal in nuclei of vehicle-treated TPCs (scale 10 μm). (**D**) Quantification of normalized nuclei with a positive signal (n=2; mean ± SEM, two-tailed paired t-test, **p<0.05). (**E**) Cytoplasmic (cyt), nuclear (nuc) and chromatin (chro) subcellular fractionation of EHMT2i-treated (as indicated) tumorspheres compared to control. Histone H4 and Tubulin are loading controls of chromatin and cytoplasmic fractions, respectively. (**F**) Chromatin immunoprecipitation using RUVBL2 antibody followed by qPCR (ChIP-qPCR) of areas flanking a *Tcf4* binding sites in promoters of the alveolar type 2 (AT2) genes *Etv5*, *Slc34a2* and *Lamp3* (n=2 mean ± SEM; *Etv5*, *Slc34a2*, two-tailed paired t-test, *p<0.05). (**G**) Representative qPCR of *Tcf4* binding motif within promoters of AT2 genes.

The online version of this article includes the following source data for figure 5:

Source data 1. Western blot for *Figure 5E* showing G9a (EHMT2) expression in subcellular fractionation of EHMT2i-treated tumorspheres compared to control.

Source data 2. Western blot for *Figure 5E* showing TUBULIN expression in middle membrane (upper band) in subcellular fractionation of EHMT2i-treated tumorspheres compared to control.

Source data 3. Western blot for *Figure 5E* showing histone H4 expression in the bottom membrane and beta catenin expression (upper membrane) in subcellular fractionation of EHMT2i-treated tumorspheres compared to control.
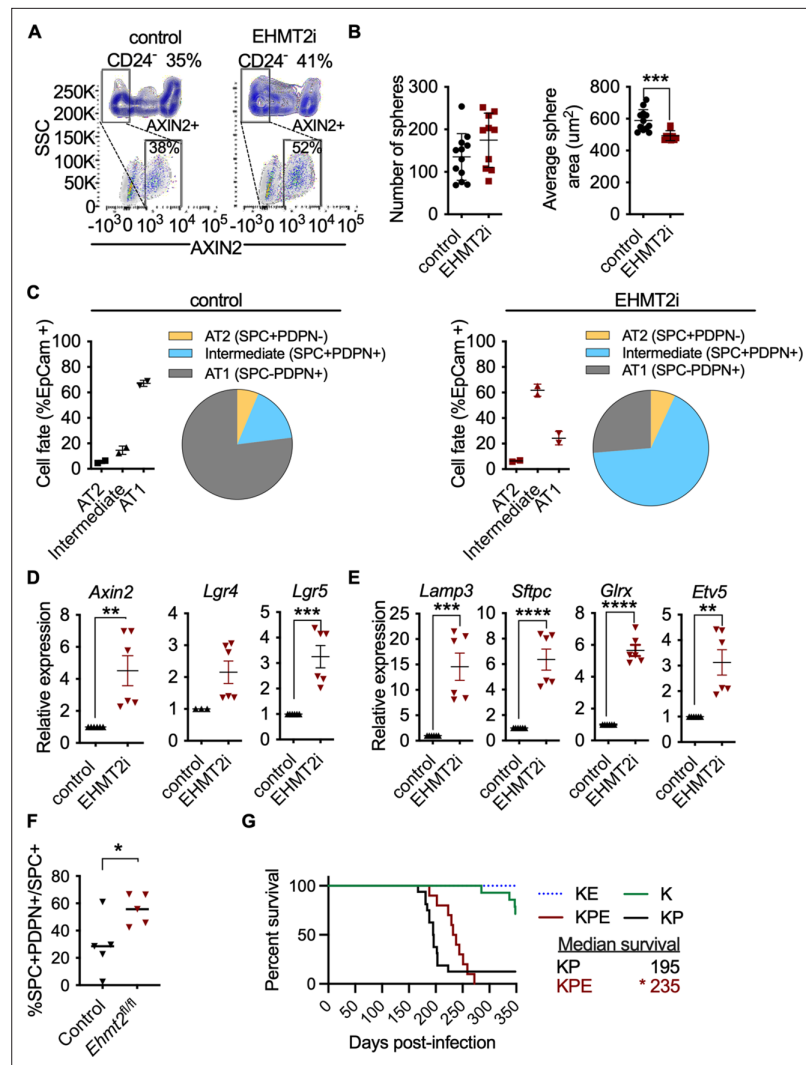
Figure 6. EHMT2 controls Wnt signaling and in AT2 cells and impairs tumor initiation. (**A**) Scatter and contour plots demonstrating intracellular staining of AXIN2 in CD24 negative (CD24⁻) epithelial cells sorted from EHMT2-inhibited mice compared to control (n=6 for each group). The blue contour plot shows gating on the CD24⁻ cell population. (**B**) Sphere number and size in alveospheres after treatment with EHMT2 inhibitor (EHMT2i) vs control. (n=10 ± SEM, two-tailed paired t-test, ***p<0.01). (**C**) Cell-lineage marker analysis of alveospheres, treated with either vehicle control or EHMT2i. Each panel shows a graph and a pie-chart depicting epithelial percentages of the AT1 marker podoplanin (PDPN) and the alveolar type 2 (AT2) marker surfactant protein C (SPC). (n=2 ± SEM), (**D**) Relative expression of *Axin2*, *Lgr4* and *Lgr5* transcripts (n=6–9 ± SEM, two-tailed paired t-test, **p<0.005, ***p<0.0001). (**E**) Relative expression of *tcf4*-containing AT2 transcript markers (n=6 ± SEM; two-tailed paired t-test, **p<0.05, ****p<0.0001). (**F**) Percentage of SPC +PDPN + double-positive cells out of SPC +in wildtype (control) (n=5) and *Ehmt2^{fl/fl}* (n=5) groups, 4 days post hyperoxic (75% O₂) injury. Quantitation represented as per-mouse, two-tailed paired t-test, *p<0.05 (**G**) Survival of *Kras^{G12D};Trp53* (KP) (n=16), *Kras^{G12D};Trp53;Ehmt2^{fl/f}* (KPE) (n=10), *Kras^{G12D}* (K) (n=14) and *Kras^{G12D};Ehmt2^{fl/f}* (KE) (n=9). Gehan-Breslow-Wilcoxon test, (*p<0.05).

The online version of this article includes the following figure supplement(s) for figure 6:

Figure supplement 1. Calibration of Axin2 antibody.

Figure supplement 2. Mean fluorescence intensity (MFI) of surfactant protein C (SPC) in alveolar type 2 (AT2) and intermediate alveosphere-derived cells, following EHMT2 inhibition vs control (n=2 ± SEM; Control (AT2) vs EHMT2i (AT2), two-tailed t-test, * p<0.05.

Figure supplement 3. Relative expression of *Ehmt2* transcript in pooled tdTomato + cells, denoting Cre exposure, from *Ehmt^{fl/fl}* vs control (n=6).

Figure 6 continued on next page

Figure 6 continued

Figure supplement 4. Representative image showing TdTomato-expressing cells a (yellow) and surfactant protein C (SPC)-expressing cells following 5 days of intratracheal infection with *AAV9-Cre*.

Figure supplement 5. Schematic representation of Hyperoxic (75% O$_2$) experiment.

Figure supplement 6. Representative images of surfactant protein C (SPC) + podoplanin (PDPN) + double positive cells.

Figure supplement 7. Decreased tumor burden in KPE mice.

by intratracheal administration of an adeno-associated virus encoding Cre (AAV9-Cre)(*Nabhan et al., 2018*). This approach allowed us to identify the EHMT2-targeted cells using a tdTomato reporter and confirm reduced EHMT2 expression from this EHMT2 -deleted population (*Figure 6—figure supplement 3*). TdT was expressed exclusively in the alveolar space and colocalized preferentially with SPC-expressing cells (*Figure 6—figure supplement 4*). To further assess how EHMT2 deletion impacts AT2 differentiation, we subsequently injured the lung using hyperoxia to promote alveolar repair (*Figure 6—figure supplement 5*). EHMT2 loss in the alveolar compartment showed a significant 2.5-fold increase in double positive (SPC + PDPN +) cells, in just 4 days following injury consistent with our ex vivo alveosphere findings (*Figure 6—figure supplement 6F*). Studies evaluating the impact of EHMT2 loss at later stages of the tissue repair process will contribute further to our understanding of its role in epithelial cell fate decisions in the lung. All together these data demonstrate that EHMT2 functions as a cell intrinsic mechanism to directly control cell fate decisions in the context of primary, untransformed AT2 cells.

The impaired regenerative capacity of AT2 cells observed by EHMT2 loss, together with the Wnt signaling effects impelled us to examine the outcome of EHMT2 deletion in Kras-dependent tumor initiation–an event that was previously shown to require cell fate alterations in other tissue contexts (*Shibata et al., 2018*). Additionally, genetic cooperativity between Ras and Wnt signaling pathways has been reported (*Juan et al., 2014*; *Pacheco-Pinedo et al., 2011*) and linked to cell fate effects. In this case, mutant beta catenin within Scgb1A1 + cells caused a distal cell fate change and enhanced tumor formation within Scgb1A1 + expressing cells (*Pacheco-Pinedo et al., 2011*). To assess the impact on tumor initiation we deleted EHMT2 using a conditional allele of the *Ehmt2* gene (*Ehmt2* $^{fl/fl}$) together with conditional *Kras*^{G12D} in the absence or presence of *Trp53* loss (KPE: *Kras*$^{lsl.G12D/wt}$: *Trp53*$^{fl/fl}$; *Ehmt2*$^{fl/fl}$ and KE: *Kras*$^{lsl.G12D/wt}$; *Ehmt2*$^{fl/fl}$) KPE mice showed a striking reduction in tumor formation and significant decrease in tumor burden in comparison to KP mice, which translated to a significant increase in overall survival (*Figure 6—figure supplement 7A,B*). Of note, the observed increase in overall survival in both KPE and KE mice was independent of p53 status. These results demonstrate that EHMT2 is crucial for Kras-mediated tumor initiation and are consistent with the requirement of EHMT2 to enable AT2 and TPC regenerative capacity and cell fate.

Discussion

Wnt signals are critical for maintaining or acquiring facultative stem-like properties in lung tissue and distinct disease contexts. Our work reveals a cell-intrinsic mechanism of Wnt pathway activation governed by EHMT2 methyltransferase activity. We find that EHMT2 inhibition directly activates transcriptional activity of chromatin-bound β-catenin within cells, revealing an intracellular mechanism of Wnt signaling control. Interestingly, we detected RUVBL2 and β-catenin interaction in both the cytoplasm and nucleus. We currently do not completely understand the role of RUVBL2-β-catenin interaction in the cytoplasm and in which subcellular compartment this interaction is regulated. One possible explanation is that RUVBL2-β-catenin complex shuttles between the nucleus and cytoplasm compartments. In the context of lung, EHMT2 activity functions to support regenerative properties of Kras^{G12D} tumors and normal AT2 cells – the predominant cell of origin of this cancer. By discovering this alternative cell-intrinsic mechanism of governing Wnt signaling in stem-like cells, we are able to manipulate cell fate decisions to predictably limit the functionality of these cells to disable tumor propagation.

The ability of AT2 stem populations to give rise to differentiated AT2 and AT1 cells is a critical feature that aids in maintaining the integrity of the distal alveolar compartment (*Nabhan et al., 2018*; *Zacharias et al., 2018*). How stemness is regulated and maintained is of considerable interest since

its dysregulation is an underlying contributor to diseases of the airway, including idiopathic pulmonary fibrosis and cancer. Wnt signaling is a master regulator of AT2 cell fate within the lung, paramount for development, homeostasis and damage repair. Regulation and tuning of Wnt signals are necessary to ensure proper repair in the alveolar compartment, but the mechanisms are context dependent. For example, β-catenin loss in AT2 cells enhances AT1 conversion, indicating Wnt signaling functionally prevents differentiation of alveolar AT2 stem cells (*Frank et al., 2016*; *Nabhan et al., 2018*). Our findings are consistent with this paradigm as functional perturbation of EHMT2 activity enhances Wnt signaling, indicating impairment of AT2 plasticity, as well as the regenerative capacity of TPCs. Of note, another report found reduced Wnt activity following EHMT2 perturbation, in three cell tumor cell lines; A549, H1299, and H1975 which invokes an APC2-mediated mechanism, albeit in a distinct cellular context from what we describe (*Zhang et al., 2018*). Indeed, the authors report that EHMT2 inhibition impairs cell growth by inhibiting Wnt. Importantly in our studies, we do not observe Wnt inhibition upon EHMT2 manipulation in either the TPC or non-TPC populations (*Figure 4A*). Additionally, the TPC population responsible for long-term regenerative capability of autochthonous tumors is not represented in established cell lines. Therefore, we view this report as a distinct context, represented by effects seen in three lung cell lines that notably all harbor mutations in ARID4A, a protein responsible for HDAC recruitment. More recent work outlines another link between EHMT2 and Wnt pathway suppression. Pal and colleagues described a role for EHMT2-mediated suppression of Wnt signaling in Rhabdomyosarcoma through activation of DKK1 (*Pal et al., 2020*). Of note, DKK1 is not expressed in AT2 cells (*Habermann et al., 2020*), thus represents a distinct mechanism of Wnt regulation from what our work describes. Although the Wnt-mediated suppression differs mechanistically from our report, this work reinforces the concept of a role for EHMT2 in suppression of Wnt signaling. Recent reports (*Nabhan et al., 2018*; *Zacharias et al., 2018*; *Zepp et al., 2017*) describe, how Wnt regulation is remarkably nuanced within the distal lung with the discovery and characterization of distinct niches that provide exogenous Wnt ligands to support neighboring stem cells. In the context of tissue damage, these interactions are likely disrupted and thereafter differentiated cells can adopt a facultative state defined by changes in Wnt signaling. Although autocrine Wnt secretion has been proposed as a mechanism to self-sustain the Wnt signaling requirements while outside of the niche, our discovery provides a means to enable cell intrinsic regulation of β-catenin transcription, providing a safe switch to maintain AT2 cell identity when a mesenchymal Wnt-providing niche, is no longer tethered to the epithelial cell.

In lung tumorigenesis, we observe that EHMT2 loss at the time of tumor initiation leads to a significant reduction in tumor formation, as well as, tumor burden resulting in significantly increased overall survival. Of note, genetic cooperativity between Ras and Wnt signaling pathways has been reported (*Juan et al., 2014*; *Pacheco-Pinedo et al., 2011*) and linked to cell fate effects. In the context of *Kras*-mutant lung tumor initiation, genetic activation of Wnt signaling using mutant beta catenin within *Scgb1A1 +* cells leads to a distal cell fate change consistent with our results. However, in contrast to our AT2-derived tumor-initiation model, mutant beta catenin expression results in enhanced tumor formation within *Scgb1A1+*expressing cells (*Pacheco-Pinedo et al., 2011*). Notably, this work differs in the cell of origin, but in that regard, it is not yet clear how distinct, alternate thresholds of Wnt signaling contribute to determining cell fate within different cell lineages in the lung. Moreover, Pacheco-Pinedo et al., used a stable form of beta catenin, whereas loss of EHMT2 activity leads to signaling of chromatin-bound beta catenin, which likely differ in both signal strength and duration. Others have reported the necessity of Wnt signaling to maintain tumors (*Juan et al., 2014*) and suggested that Wnt gradients might be critical for self-renewal, in line with the necessity for a specific Wnt threshold to support this process (*Tammela et al., 2017*). Of note, a recent report surprisingly demonstrated enhanced tumor formation when initiating tumors with mutant Kras and EHMT2 knockdown (*Rowbotham et al., 2018*), This is in direct contradiction to our findings using a genetic model to delete EHMT2 concurrent with *Kras^{G12D}* in tumor initiation. Importantly, the shRNA seed sequence used in the Rowbotham study targets nine other target transcripts with 100% homology in addition to *Ehmt2* (*Supplementary file 1*), raising the possibility that genes other than *Ehmt2* may be implicated in the described phenotype. Notably, one of the genes targeted by this shRNA construct is *Babam1*, which is known to increase the metastatic capability of a murine Kras-mutant lung cancer-derived cell line (*Chen et al., 2015*), (*Supplementary file 1*). While in contrast to our findings, these technical differences preclude definitive conclusions from those experiments within their study.

Our work implicates EHMT2 as an important mediator of Wnt signals in order to maintain tumor propagating capacity. This cell autonomous mechanism for activating Wnt signaling may be beneficial in contexts of tumor seeding and regrowth, allowing independence from niche factors. EHMT2 activity functions similarly in primary AT2, as well as, *Kras*-transformed tumor cells, suggesting that TPCs may share functional features of their respective cell of origin. The discovery that EHMT2 functions to directly regulate Wnt signaling deepens our mechanistic understanding of EHMT2 activity and presents potential opportunities for targeting in both lung cancer, as well as other AT2-mediated lung pathologies.

Materials and methods

Key resources table

Reagent type (species) or resource	Designation	Source or reference	Identifiers	Additional information
Cell lines (Homo-sapiens)	A549	ATCC	CRM-CCL-185	Short tandem repeat profiling, SNP fingerprinting, and mycoplasma testing were used for strict quality control.
Cell lines (Homo-sapiens)	MRC5	ATCC	CCL-171	Short tandem repeat profiling, SNP fingerprinting, and mycoplasma testing were used for strict quality control.
Cell lines (Homo-sapiens)	RKO	ATCC	CRL-2577	Short tandem repeat profiling, SNP fingerprinting, and mycoplasma testing were used for strict quality control.
Antibody	(rat monoclonal); CD45 biotin conjugated	BD Biosciences	553078; clone 20-F11	(1:200)
Antibody	(rat monoclonal);Ter119 biotin conjugated	BD Biosciences	553672; clone Ter119	(1:200)
Antibody	(goat polyclonal); clone MEC13.3; CD31 biotin conjugated	BD Biosciences	553371	(1:200)
Antibody	(rat monoclonal); CD24 PerCP-eFluor 710	eBioscience	46–0242	(1:300)
Antibody	(rat monoclonal); EPCAM-FITC	Biolegend	118208; Clone G8.8	(1:20)
Antibody	(rat monoclonal); ITGB4-PE	Biolegend	123602; clone 346–11 A	(1:20)
Antibody	(armenian hamster monoclonal); Notch1-APC	Biolegend	130613; clone HMN1-12	(1:80)
Antibody	(armenian hamster monoclonal); Notch2-APC	Biolegend	130714; clone HMN2-35	(1:80)
Antibody	(armenian hamster monoclonal); Notch3-APC	eBioescience	17-5763-82; clone HMN3-133	(1:80)
Antibody	(armenian hamster monoclonal); Notch4-APC	Biolegend	128413; clone HMN4-14	(1:80)
Antibody	(rat monoclonal); Fc-Block	BD Biosciences	553141; clone 2.4 /G2	(1:1000)
Antibody	(mouse monoclonal); CD74-BUV395	BD Biosciences	740274; clone ln-1	(1:25)
Antibody	(rabbit polyclonal); Pro-SPC	Abcam	ab170699	(1:200)
Antibody	(rabbit monoclonal); G9a	Abcam	ab185050; clone EPR18894	(1:1000)
Antibody	(mouse monoclonal); Podoplanin	ThermoFisher	MA5-16113; clone 8.1.1	(1:200)
Antibody	(rabbit polyclonal); Alexa Fluor 488	ThermoFisher	A-21206	(1:500)

Continued on next page

eLife Research article

Cancer Biology | Cell Biology

Continued

Reagent type (species) or resource	Designation	Source or reference	Identifiers	Additional information
Antibody	(mouse monoclonal); BrdU	NeoMarkers	MS-1058-PO; clone BRD.3	(1:200)
Antibody	(mouse monoclonal); Cleaved Caspase-3	Cell signaling Technology	9661	(1:300)
Antibody	(rabbit polyclonal); CC10	SantaCruz Biotechnology	9772	(1:200)
Antibody	(mouse monoclonal); FoxJ1	eBioscience	14-9965-82; clone 2A5	(1:25)
Antibody	(rat monoclonal); Rage	R&D Systems	175410; clone MAB1179	(1:100)
Antibody	(mouse monoclonal); Actin	BD Biosciences	612656; clone C4	(1:20,000)
Antibody	(rabbit polyclonal); Axin2	Abcam	109307; clone EPR2005	(1:100)
Antibody	(mouse monoclonal); H3K9me2	Abcam	Ab1220	(1:1000)
Antibody	(rabbit polyclonal); RUVBL2	Bethyl Laboratories	A302-536	Western
Antibody	(mouse monoclonal); Beta-catenin	BD Biosciences	610153	Western
Antibody	(rabbit polyclonal); H3K9me3	Active Motif	39161	(1:1000)
Antibody	(mouse monoclonal); Histone H3	Cell Signaling Technology	3638; clone 96C10	(1:1000)
Antibody	(rabbit polyclonal); RUVBL2	Bethyl Laboratories	A5302-537A	Immunoprecipitation
Antibody	(rabbit polyclonal); Beta-catenin	ThermoFisher	71–2700	Immunoprecipitation
Chemical compound, drug	PE/Cy7 Streptavidin	Biolegend	405206	(1:300)
Chemical compound, drug	UNC0642	Biotechne	5132	
Chemical compound, drug	CHIR99021	Biotechne	4423	
Commercial assay, kit	Matrigel	Corning	356231	
Commercial assay, kit	Dynabeads Co-IP kit	ThermoFisher	14–321	
Commercial assay, kit	PerfeCTa	QuantaBio	95146–005	
Commercial assay, kit	True-ChIP Kit	Diagenode	C01010140	
Commercial assay, kit	SAGM media	Lonza	CC-3118	
Commercial assay, kit	Collagenase/Dispase	Roche	COLLD-RO	2 ug/ml final concentration
Transfected construct (bacteriophage P1)	Adeno CMV-Cre	Baylor College of Medicine	Adeno CMV-Cre	Concentration 1.2 × 107 plaque-forming units
Transfected construct (bacteriophage P1)	Adeno-Flp-Ires-Cre	Baylor College of Medicine	Adeno-Flp-Ires-Cre	Concentration 1.2 × 107 plaque-forming units
Transfected construct (bacteriophage P1)	AAV9-Cre	Virovek	AAV9-Cre	2E13 vg/ml dilution 1:60 in 60 ul vol.
Other	Bioruptor Pico	Diagenode	B01080010	
Other	Influx cell sorter	BD Biosciences	NA	
Software, algorithm	Flowjo	BD Biosciences	Flowjo.com	
Software, algorithm	ImageJ	ImageJ	https://imagej.nih.gov/ij/	

Reagent type (species) or resource	Designation	Source or reference	Identifiers	Additional information

Primer sequences included in **Supplementary file 2**.
SPC: surfactant protein C.

Mice

Kras[LSL-G12D] (**Jackson et al., 2001**), *Trp53*[flox/flox] (**Jonkers et al., 2001**), *Trp53*[frt/frt] (**Lee et al., 2012**), *Rosa26*[LSL-tdTomato] (**Madisen et al., 2010**) were licensed by Genentech Inc All animal studies were approved by the Institutional Animal Care and Use Committee at Genentech and adhere to the Guidelines for the Care and Use of Laboratory Animals (protocols 17–1217, 17–0107, and 18–1833 series). Tumors were induced in KP mice at 8–12 weeks of age using intranasal infection of AdCMV-Cre or Adeno-Flp-IRES-Cre (Baylor College of Medicine) at 1.2×10^7 plaque-forming units (PFU). In vivo treatment with EHMT2 inhibitor UNC0642 was performed by treating mice with either vehicle (60% PEG400/40% $H_2$0) or with UNC0642 10 mg/kg, IP, daily (60% PEG400/40% $H_2$0) for a duration of 6 days. Lungs were harvested and sorted for CD24^{-} as previously described (**Barkauskas et al., 2013**; **McQualter et al., 2010**). For in vivo dosing experimentation of models, animals were randomized into treatment cohorts by tumor measurement, with equal numbers of male and female animals. The animals were dosed and monitored according to guidelines from the IACUC at Genentech, Inc Animals were censored for survival in an unblinded manner based on predetermined morbidity criteria.

Ehmt2 conditional knockout design

Ehmt2 expression vector was constructed by introducing a Frt-PGK-em7-NEO-Frt as a selection marker. LoxP sites were introduced into the 5' and 3' homology sequences flanking the targeted exons (genomic location 34908772–34912090 and 34916244–34918676, respectively). The loxP sites, flanked exon 25–27, constituting the SET catalytic domain of *Ehmt2*. 5' and 3' extra genomic regions were used to design PCR primers to validate the targeted deletion which generates a 2.2 kb fragment upon Cre recombinase administration. Conditional gene deletion in the adult was generated in the lung upon Adeno-Cre administration. Licensing and strain availability upon request from Genentech (**Scheme 1**).
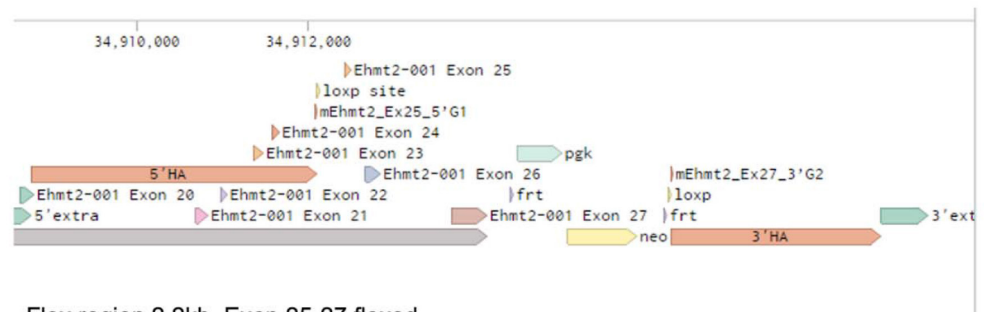
Scheme 1. Ehmt2 CKO-Genomic Structure.

Orthotopic transplantation studies

For tumor formation, 8–12 week-old recipient mice were intratracheally transplanted with 25,000–45,000 inducible shRNA-carrying primary KP tumor cells per mouse. Cells were resuspended in 60 μL MEM alpha (Gibco) before transplantation and monitored using micro CT as previously described (**Zheng et al., 2013**).

Cell isolation and tumorsphere preparation

Pooled KP tumors from 3 to 6 mice per experiment, were extracted out of the lung and completely minced with a razor blade. The material was resuspended in DMEM-F12 media containing 10% fetal bovine serum (FBS), 1 × P/S and 2 µg/ml collagenase-dispase in 50 ml conical tubes and incubated for 1–1.5 hr in a 37°C incubator on a shaking platform. Digested material was sequentially filtered through 70 micron and 40 micron strainers, distributed into 15 ml conical tubes and centrifuged for 5 min at 500 g. Pellets were resuspended in hypotonic lysis buffer (15 mM NH_4Cl, 10 mM $KHCO_3$, and 0.1 mM EDTA) for 1–2 min, neutralized with DMEM-F12 and spun down on a 1 ml FBS cushion to remove cell debris. Final cell pellets were resuspended in PBS containing 10% FBS. For tumorsphere assays, KP tumor cells were mixed with Matrigel in tumorsphere media as previously described (*Zheng et al., 2013*). TPCs were sorted and analyzed using the influx machine (BD). Sorting was performed as previously described by *Zheng et al., 2013* with the following modifications. Immune cell lineage content was excluded by sorting with the following antibodies: biotin-conjugated CD45 (BD, 553078, 30-F11,1:200), CD31(BD, 553371, MEC13.3, 1:200), Ter119 (BD, 553672, Ter119, 1:200), thereafter biotin-conjugated antibodies were detected with phycoerythrin (PE)/Cy7 streptavidin (Biolegend, 405206: 1:300), and subsequently stained for EpCAM +FITC (Biolegend, 118208, G8.8, 1:20) and TPC markers CD24 PerCP-eFluor 710 (eBioscience, 46–0242, M1/69: 1:300), ITGB4-PE (Biolegend, 123602, 346–11 A, 1:20) and Notch1 (Biolegend, 130613, HMN1-12, 1:80), Notch2 (Biolegend, 130714, HMN-2–35, 1:80), Notch3 (eBioescience, 17-5763-82, HMN3-133, 1:80), Notch4 (Biolegend, 128413, HMN4-14, 1:80). All anti-notch antibodies are allophycocyanin (APC) conjugated and used as a pool.

Transduction of primary KP tumor cells

shRNAs containing the following *Ehmt2* hairpins shG9.1: 5' acagcaagtctgaagtcgaa 3', shG9a.2: 5' cact gtcaccgtcggcgatga 3' were synthesized, cloned into a mirE backbone and then subsequently sub-cloned into pInducer-10 (*Fellmann et al., 2013*; *Meerbrey et al., 2011*) and transfected with pack-aging constructs into 293T cells using Lipofectamine 2000 (Thermo Fisher). Viral supernatants were collected 72 hr-post transfection and subsequently concentrated using ultracentrifuge at 25,000 RPM for 2 hr to generate high-titer virus. Freshly-sorted primary KP tumor cells were infected over-night using ultra-low attachment plates (corning) and subsequently transplanted or grown in Matrigel as tumorspheres.

TPC gating strategy

Cells and doublet cells were excluded from the sort, respectively. EpCAM-Lineage scatter plot was used to gate on epithelial cells. Each TPC marker was gated in an individual scatter plot against a mock gate in the following sub-gating scheme: CD24 + cells gated from EpCAM + cells, ITGB4 + cells gated from CD24 + cells and Notch^{HI} gated from ITGB4 + cells. Non-TPCs were classified as the 'non-positive' cells for each individual marker scheme and gated accordingly. All non-TPC were combined in one single tube.

Tumorsphere and TPC assays

For EHMT2 inhibition assays in KP tumorspheres, 10,000–20,000 KP primary tumor cells from 3 to 6 mice for each biological replicate were seeded in Matrigel for 4–5 days before treatment. Each biological replicate contained n=3–4 technical replicates. Tumorspheres were then treated with either vehicle or 2 µM of the EHMT2 inhibitor Unc0642 (Bio-techne) for an additional 5–7 days. For Wnt acti-vation assays, established tumorspheres were treated with either 0.5 µM or 3 µM CHIR99021 (Tocris) for 5 days. For EHMT2 inhibition assays in TPCs, 5×10^6–10×10^6 KP primary tumor cells from 6 to 8 mice per experiment were seeded per 5 ml Matrigel plug for 4–5 days before treatment and treated as described above. Cells were then extracted out from Matrigel as single cell suspensions and sorted for the TPC cell subset. TPC isolation directly from treated or untreated cultured tumorspheres was performed using the influx sorter (BD).

Secondary sphere formation assays

For secondary sphere formation assays following EHMT2 inhibition or depletion, established KP tumor-spheres were mechanically and enzymatically dissociated with 2 µg/ml collagenase/Dispase (Roche).

To obtain single-cell suspensions, dissociated KP tumorspheres were further treated with Accutase (Corning) for 5–10 min, counted and re-seeded in Matrigel in 3–4 technical replicates per experiment. Matrigel, spheres were then counted using a 10×20 eyepiece containing 0.5×0.5 mm grid.

Alveolar and AT2-derived alveosphere preparations

AT2 derived alveosphere assays were generated by isolating Epcam$^+$/CD24$^-$ cells as previously described (*Barkauskas et al., 2013*; *McQualter et al., 2010*). Sorted cells were either intracellularly stained for Axin2 Abcam (109307, EPR2005, 1:100) or alternatively, resuspended in SAGM media (Lonza) and mixed in a 1:1 ratio with growth factor-reduced Matrigel (BD Biosciences). 100 µl of mixed cells/Matrigel suspension was placed in 24-well Transwell inserts (Falcon) and allowed to solidify. To allow alveospheres growth, 5×10^4 MRC5 human lung fibroblasts (ATCC CCL-171) were seeded in the bottom chamber supplied with 500 µl MTEC media. Media was changed every other day. EHMT2 inhibitor was replaced every 2–3 days.

Tumorsphere immunofluorescence (IF)

KP tumorspheres were either stained in Matrigel or were paraffin-embedded, sectioned and stained as previously described (*Huber et al., 2015*). For Matrigel preparations, tumorspheres were fixed in 4% PFA for 40 min, washed 3×5 min, permeabilized with 0.5% Triton X-100 for 30 min then blocked in 4% BSA for 30–60 min. Staining was performed in blocking buffer with 0.05% Triton X-100 and washes were performed with 0.1% Triton X-100. Tumorspheres were imaged using a Leica SPE confocal microscope. The following antibodies were used for IF: BrdU (NeoMarkers, MS-1058-PO, BRD.3 1:200), cleaved caspase-3 (Cell Signaling Technology, 9661 1:300) pro-SPC (Abcam, ab170699: 1:200), CC10 (SantaCruz, 9772, 1:200) FoxJ1 (eBioscience, 14-9965-82, 2A5), RAGE (R&D, 175410, MAB1179, 1:100).

BrdU incorporation in tumorspheres

BrdU labeling reagent (ThermoFisher) was incorporated for 3 hr. Tumorspheres were then processed according to IF procedures described in the previous section.

Quantification of tumorsphere IF images

Images were taken using SP5 Confocal (Leica). Single projection images of 4–6 z-stack sections from at least 15–20 tumorspheres were constructed and analyzed in the Matlab software package (version R2016b by Mathworks, Natick, MA). Individual cell nuclei were segmented using regional intensity maxima and watershed thresholding on the DAPI channel, and then scored by the presence of relevant IF signal above a global intensity threshold in the area immediately surrounding each nucleus. For BrdU images, signal was calculated in each nucleus around intensity maxima. Quality control images were also created by superimposing the cell scoring mask on the raw image data.

IP and chromatin immunoprecipitation (ChIP)

For Co-IP experiments β-catenin and RUVBL2 were pulled-down from vehicle or EHMT2 inhibitor-treated A549, using Thermo Fisher (71–2700) or Bethyl (A5302-537A) antibodies, respectively, and utilizing the Dynabeads Co-IP kit (14-321) as indicated by protocol. To detect interacting proteins, membrane was blotted for β-catenin BD (610153) or RUVBL2 Bethyl (A302-536A). ChIP experiments were performed on tumor propagating cells (TPCs) sorted directly from vehicle or EHMT2 inhibitor treated-tumorspheres using the Diagenode True-ChIP protocol (C01010140) with the following modifications. Briefly, 50 K-100K cells were crosslinked with 1% formaldehyde for 8 min, chromatin was sheared to 100–500 bp fragments using the Bioruptor Pico sonicator for 3 cycles of 30 s on/off in 0.5 ml tubes (Diagenode). Quantitation of chromatin was performed using a qubit fluorimeter where at least 10 ng of chromatin were used per experiment. Pulldown was performed with 0.5 ug RUVBL2 antibody Bethyl (A302-537A) overnight then incubated with 30 min preblocked protein A conjugated Dynabeads. Immunoprecipitated material was then washed as indicated by protocol with an additional LiCl buffer wash (0.25 M LiCl, 1% IGEPAL, 1% deoxycholic acid, 1 mM EDTA, 10 mM Tris, pH 8.1). Samples corss-links where then reversed and then samples were preamplified using PerfeCTa, QuantaBio (95146–005). The precipitated DNA and input DNA were quantified by qPCR using specific primers flanking a TCF4 binding site in the promoters of the following genes, *Etv5, Slc34a2, Lamp3*.

Cell lineage marker analysis

Mouse cell lineage markers were obtained from *Treutlein et al., 2014* using the following selection criteria: Pearson correlation ≥ 0.5, p-value (GBA, BH corrected)<0.05. This resulted in 30 mouse genes characteristic of AT1 cells, 28 genes for AT2 cells, 43 genes for Club cells, and 84 genes for ciliated cells. The biomaRt R package was used to map mouse genes to human orthologs, resulting in 28 human AT1 markers, 26 AT2 markers, 39 club markers, and 65 ciliated markers. For the assessment of lineage markers in human and mouse samples, expression data Z scores were first calculated for each gene across the 546 human LUAD tumors, and across the 10 mouse KP tumorsphere samples. Cell lineage signature scores were then calculated for human adenocarcinoma tumors as the average z-score expression of the human markers for each cell lineage and for mouse samples as the weighted average z-scored expression of the mouse markers with weights set to $-\log^{10}$(p-value). P-values were obtained from Table S4 (*Treutlein et al., 2014*).

Transmission Electron microscopy (TEM)

Lung tumorspheres were first fixed in modified Karnovsky's fixative and then post-fixed in freshly prepared 1% aqueous potassium ferrocyanide-osmium tetroxide (EM Sciences, Hatfield, PA), for 2 hr followed by overnight incubation in 0.5% Uranyl acetate at 4^0C. The samples were then dehydrated followed by propylene oxide (each step was for 15 min) and embedded in Eponate 12 (Ted Pella, Redding, CA). Ultrathin sections (80 nm) were cut with an Ultracut microtome (Leica), stained with 0.2% lead citrate and examined in a JEOL JEM-1400 TEM at 80kV. Digital imaged were captured with a GATAN Ultrascan 1000 CCD camera. For each biological replicate, 20 randomly selected cells in each treatment were manually scored and quantified for lamellar bodies. Sections were imaged at low and high magnifications, scale bars 2 μm and 0.5 μm, respectively.

qRT-PCR analysis

RNA isolation for tumorspheres was performed using the RNAeasy Micro plus kit (Qiagen). Tumorspheres were dissociated as described. Samples were then measured using nanodrop and subsequently reverse transcribed using SuperScript III (ThermoFisher). For TPCs an additional step of pre-amplification was performed using TaqMan Preamp Master Mix (ThermoFisher). qRT-PCR was performed using fast advanced PCR Master Mix (ThermoFisher). *Hprt* and *Actin* were used as reference genes for all assays. All Taqman Assays used in the study are described in *Supplementary file 2*.

Tumorsphere subcellular fractionation

Pooled primary KP tumorspheres (n=6) from EHMT2-treated and control Matrigel cultures were extracted, fractionated and processed to generate cytoplasmic, nuclear and chromatin fractions, using Subcellular Protein Fractionation Kit Thermo Fisher (78840), as defined by the protocol.

Antibody validation assays

Axin2 validation was conducted using both human RKO cells and intestinal sections of *APC^loxp/loxp* vs *APC^fl/fl*; *ROSA26^CreERT2*. Briefly, RKO cells were GSK3-β (CHIR)-treated for 48 hr vs controls, harvested, 4% paraformaldehyde fixed for 10 min and subsequently washed and permeabilized with 0.25% Triton X-100. Cells were then blocked with 2.5% horse serum and stained for Axin2 Abcam (ab109307, EPR2005, 1:100) for flow cytometry. Intestinal epithelial sections were stained with Axin2 (ab109307, EPR2005, 1:25, AR; Citrate pH = 6).

Western blot for TPCs and tumorspheres

TPCs and non-TPCs were sorted from 60 tumor-bearing mice to generate material for Western. Whole cell extracts were lysed in RIPA buffer (50 mM Tris-HCl, 150 mM NaCl, 1% Deoxycholate 0.1% SDS 1% Triton-X100) supplemented with Halt protease and phosphatase inhibitor cocktails (ThermoFisher). Lysates were quantified using pierce BCA protein assay kit (Pierce). To detect histones in tumorspheres, acid extraction method was used as previously described (*Shechter et al., 2007*). Antibodies used for Western blotting of TPCs and non-TPCs: G9a (Abcam, ab185050, EPR18894, 1:1000), Actin (BD, 612,656, C4, 1:20,000), was used as loading control. In tumorspheres; H3K9me2 (Abcam, Ab1220, 1:1000), H3K9me3 (Active Motif, 39,161 1:1000) histone H3 (cell signaling technology, 3638, 96C10, 1:1000), was used as loading control.

RNA-sequencing data for tumorspheres

5 biological repetitions of primary tumorspheres were generated from pooled KP tumors from 6 to 10 mice per experiment. In each experiment matched KP tumorspheres were treated with either vehicle or G9a inhibitor (UNC0642). Total RNA was extracted using Qiagen RNeasy kit as per the manufacturer's protocol and quality control of RNA samples was performed to determine their quantity and quality. The concentration of RNA samples was determined using NanoDrop 8000 (Thermo Scientific) and the integrity of RNA was determined by fragment analyzer (Advanced Analytical Technologies). 0.5–100 ng of total RNA was used as an input for library preparation using TruSeq RNA Sample Preparation Kit v2 (Illumina). Size of RNA-seq libraries was confirmed using 4200 TapeStation and high sensitivity D1K screen tape (Agilent Technologies). Library concentration was determined by a qPCR-based method using library quantification kit (KAPA). The libraries were multiplexed and then sequenced on Illumina HiSeq4000 (Illumina) to generate 30 M of single end 50 base pair reads.

RNA sequencing data were analyzed with HTSeqGenie (*Pau et al., 2012*) in BioConductor (*Huber et al., 2015*) as follows: first, reads with low nucleotide qualities (70% of bases with quality <23) or rRNA and adapter contamination were removed. Reads were then aligned to the reference genome GRCm38 using GSNAP (*Wu and Nacu, 2010*). Alignments that were reported by GSNAP as 'uniquely mapping' were used for subsequent analysis. Gene expression levels were quantified as reads per kilobase of exon model per million mapped reads normalized by size factor (nRPKM), defined as number of reads aligning to a gene in a sample/(total number of uniquely mapped reads for that sample × gene length × size factor).

Assay for transposase-accessible chromatin using sequencing (ATAC-Seq)

Cells were aliquoted into cryovials, frozen, and shipped to Epinomics, Menlo Park, CA. Cells were processed as previously described (*Buenrostro et al., 2013*). Paired-end reads were aligned to mouse reference genome GRCm38 using GSNAP (*Wu and Nacu, 2010*) version '2013-10-10', allowing a maximum of two mismatches per read sequence (parameters: '-M 2 n 10 -B 2 -I 1–pairmax-dna=1000–terminal-threshold=1000–gmap-mode=none–clip-overlap'). Duplicate reads and reads aligning to locations in the mouse genome containing substantial sequence homology to the mitochondrial chromosome or to the ENCODE consortium blacklisted regions were omitted from downstream analyses. Remaining aligned reads were used to quantify chromatin accessibility according to the ENCODE pipeline standards with minor modifications as follows. Accessible genomic locations were identified by calling peaks with MACS 2.1.0 (*Zhang et al., 2008*) using insertion-centered pseudo-fragments (73 bp–community standard) generated on the basis of the start positions of the mapped reads and a width of 250 bp. Accessible peak locations were identified as described; briefly, we called peak significance (cutoff of P=1e-7) on a condition-level pooled sample containing all pseudo-fragments observed in all replicates within each condition. Peaks in the pooled sample, independently identified as significant (cutoff P=1e-5) in two or more of the constituent biological replicates were retained, using the union of all condition-level reproducible peaks to form the atlas. (https://www.encodeproject.org/atac-seq/). The atlas consisted of 184,032 peaks with a median width of 266 bp (ranging from 250 bp to 1531 bp). 20.4% of peaks were located in promoter regions, 32.6% in intergenic regions, and 43.3% in introns.

Chromatin accessibility within each peak for each replicate was quantified as the number of pseudo-fragments overlapping a peak and normalized these estimates using the TMM method (*Robinson and Oshlack, 2010*). Differentially accessible peaks between control and EHMT2 -inhibited samples were identified using the framework of a linear model, accounting for TPC and non-TPC and implemented with the edgeR R package. Significant differences in chromatin accessibility levels within a peak between EHMT2 i-treated and control-treated samples was set to log2-fold change >1.5 and FDR <0.05. The fold-change of ATAC-seq peaks were used as input for gene set enrichment analysis using the Hallmark MsigDB gene set collection, v6.1 (*Liberzon et al., 2015*).The integrative genomics viewer (IGV) was used for visualization of ATAC-seq peaks near genes of interest (*Robinson et al., 2011*). All source code and sequencing data are available at https://github.com/anneleendaemen/G9a.CellIdentity.Lung; *Pribluda, 2020*.

Cancer genome atlas (TCGA) RNA-sequencing data analysis

RNA-sequencing (RNAseq) data for 546 LUAD tumors from TCGA (*Cancer Genome Atlas Research, 2014*) were obtained from the National Cancer Institute Genomic Data Commons (https://gdc.cancer.gov). We employed the same approach for RNAseq data processing and quantification, with human reference genome GRCh38.

Motif enrichment near lineage markers

For each cell lineage, function findMotifs.pl from HOMER 4.7 (*Heinz et al., 2010*) was used to identify enriched motifs near cell lineage markers from *Treutlein et al., 2014*. Motif enrichment was performed with promoter regions defined from –2000 bp to 500 bp relative to TSS, and with the background sets defined as the full genome. Locations of the TCF4 motif near cell lineage markers (from –2000 bp to 500 bp relative to TSS) were determined using findMotifs.pl from HOMER 4.7. The TCF4 motif file was obtained from the HomerMotifDB (http://homer.ucsd.edu/homer/motif/HomerMotifDB/homer-Results.html).

Additional information

Author contributions

Ariel Pribluda, Conceptualization, Formal analysis, Investigation, Methodology, Writing – original draft, Writing – review and editing; Anneleen Daemen, Marc Hafner, Formal analysis, Investigation, Methodology; Anthony Nelson Lima, Oded Foreman, Julia T Garcia, Investigation; Xi Wang, Investigation, Methodology; Chungkee Poon, Methodology; Zora Modrusan, Benjamin Haley, Resources, Methodology; Anand Kumar Katakam, Formal analysis, Methodology; Jefferey Eastham, Jefferey Hung, Formal analysis; Erica L Jackson, Supervision, Writing – review and editing; Melissa R Junttila, Conceptualization, Supervision, Writing – original draft, Writing – review and editing

Author ORCIDs

Ariel Pribluda ⬤ http://orcid.org/0000-0003-2817-2827
Anneleen Daemen ⬤ http://orcid.org/0000-0001-6287-7105
Marc Hafner ⬤ http://orcid.org/0000-0003-1337-7598
Erica L Jackson ⬤ http://orcid.org/0000-0002-7100-8021
Melissa R Junttila ⬤ http://orcid.org/0000-0003-3538-1192

Ethics

All animal studies were approved by the Institutional Animal Care and Use Committee at Genentech and adhere to the Guidelines for the Care and Use of Laboratory Animals (protocols 17-1217, 17-0107 and 18-1833 series).

Decision letter and Author response

Decision letter https://doi.org/10.7554/eLife.57648.sa1
Author response https://doi.org/10.7554/eLife.57648.sa2

Additional files

Supplementary files

• Supplementary file 1. Summary of transcripts with 100% sequence identify to shEhmt2a seed sequence reported in *Rowbotham et al., 2018*. The seed for sh*Ehmt2* was queried in NCBI BLAST and the resulting query results are shown.

• Supplementary file 2. Primer sequences.

• MDAR checklist

Data availability

All source code used in this study has been made available in the R computer language, in a fully documented software and data package. This package is freely available under the Creative Commons 3.0 license and can be downloaded from https://github.com/anneleendaemen/G9a.CellIdentity.Lung, (copy archived at swh:1:rev:207a6bd1022c199eaae3ef0d2fcc9e4edcbb3c69).

The following previously published datasets were used:

Author(s)	Year	Dataset title	Dataset URL	Database and Identifier
Treutlein	2014	High throughput quantitative whole transcriptome analysis of distal mouse lung epithelial cells from various developmental stages (E14.5, E16.5, E18.5 and adult)	https://www.ncbi.nlm.nih.gov/geo/query/acc.cgi?acc=GSE52583	NCBI Gene Expression Omnibus, GSE52583
The cancer genome atlas	2014	Comprehensive molecular profiling of lung adenocarcinoma	https://tcga-data.nci.nih.gov/docs/publications/luad_2014/	tcga-data, luad_2014

References

Balis JU, Conen PE. 1964. The role of alveolar inclusion bodies in the developing lung. *Laboratory Investigation; a Journal of Technical Methods and Pathology* **13**:1215–1229 PMID: 14212352.

Barkauskas CE, Cronce MJ, Rackley CR, Bowie EJ, Keene DR, Stripp BR, Randell SH, Noble PW, Hogan BLM. 2013. Type 2 alveolar cells are stem cells in adult lung. *The Journal of Clinical Investigation* **123**:3025–3036. DOI: https://doi.org/10.1172/JCI68782, PMID: 23921127

Batlle E, Clevers H. 2017. Cancer stem cells revisited. *Nature Medicine* **23**:1124–1134. DOI: https://doi.org/10.1038/nm.4409, PMID: 28985214

Bauer A, Chauvet S, Huber O, Usseglio F, Rothbächer U, Aragnol D, Kemler R, Pradel J. 2000. Pontin52 and reptin52 function as antagonistic regulators of beta-catenin signalling activity. *The EMBO Journal* **19**:6121–6130. DOI: https://doi.org/10.1093/emboj/19.22.6121, PMID: 11080158

Beck B, Blanpain C. 2013. Unravelling cancer stem cell potential. *Nature Reviews. Cancer* **13**:727–738. DOI: https://doi.org/10.1038/nrc3597, PMID: 24060864

Buenrostro JD, Giresi PG, Zaba LC, Chang HY, Greenleaf WJ. 2013. Transposition of native chromatin for fast and sensitive epigenomic profiling of open chromatin, DNA-binding proteins and nucleosome position. *Nature Methods* **10**:1213–1218. DOI: https://doi.org/10.1038/nmeth.2688, PMID: 24097267

Cancer Genome Atlas Research N. 2014. Comprehensive molecular profiling of lung adenocarcinoma. *Nature* **511**:543–550. DOI: https://doi.org/10.1038/nature13385, PMID: 25079552

Chen M-W, Hua K-T, Kao H-J, Chi C-C, Wei L-H, Johansson G, Shiah S-G, Chen P-S, Jeng Y-M, Cheng T-Y, Lai T-C, Chang J-S, Jan Y-H, Chien M-H, Yang C-J, Huang M-S, Hsiao M, Kuo M-L. 2010. H3K9 histone

methyltransferase g9a promotes lung cancer invasion and metastasis by silencing the cell adhesion molecule ep-CAM. *Cancer Research* **70**:7830–7840. DOI: https://doi.org/10.1158/0008-5472.CAN-10-0833, PMID: 20940408

Chen X, Skutt-Kakaria K, Davison J, Ou Y-L, Choi E, Malik P, Loeb K, Wood B, Georges G, Torok-Storb B, Paddison PJ. 2012. G9a/GLP-dependent histone h3k9me2 patterning during human hematopoietic stem cell lineage commitment. *Genes & Development* **26**:2499–2511. DOI: https://doi.org/10.1101/gad.200329.112, PMID: 23105005

Chen S, Sanjana NE, Zheng K, Shalem O, Lee K, Shi X, Scott DA, Song J, Pan JQ, Weissleder R, Lee H, Zhang F, Sharp PA. 2015. Genome-wide CRISPR screen in a mouse model of tumor growth and metastasis. *Cell* **160**:1246–1260. DOI: https://doi.org/10.1016/j.cell.2015.02.038, PMID: 25748654

Collins R, Cheng X. 2010. A case study in cross-talk: the histone lysine methyltransferases g9a and GLP. *Nucleic Acids Research* **38**:3503–3511. DOI: https://doi.org/10.1093/nar/gkq081, PMID: 20159995

de Lau W, Barker N, Low TY, Koo B-K, Li VSW, Teunissen H, Kujala P, Haegebarth A, Peters PJ, van de Wetering M, Stange DE, van Es JE, Guardavaccaro D, Schasfoort RBM, Mohri Y, Nishimori K, Mohammed S, Heck AJR, Clevers H. 2011. Lgr5 homologues associate with wnt receptors and mediate R-spondin signalling. *Nature* **476**:293–297. DOI: https://doi.org/10.1038/nature10337, PMID: 21727895

Desai TJ, Brownfield DG, Krasnow MA. 2014. Alveolar progenitor and stem cells in lung development, renewal and cancer. *Nature* **507**:190–194. DOI: https://doi.org/10.1038/nature12930, PMID: 24499815

Domen J, Weissman IL. 1999. Self-renewal, differentiation or death: regulation and manipulation of hematopoietic stem cell fate. *Molecular Medicine Today* **5**:201–208. DOI: https://doi.org/10.1016/S1357-4310(99)01464-1, PMID: 10322312

Easwaran H, Tsai HC, Baylin SB. 2014. Cancer epigenetics: tumor heterogeneity, plasticity of stem-like states, and drug resistance. *Molecular Cell* **54**:716–727. DOI: https://doi.org/10.1016/j.molcel.2014.05.015, PMID: 24905005

Epsztejn-Litman S, Feldman N, Abu-Remaileh M, Shufaro Y, Gerson A, Ueda J, Deplus R, Fuks F, Shinkai Y, Cedar H, Bergman Y. 2008. De novo DNA methylation promoted by g9a prevents reprogramming of embryonically silenced genes. *Nature Structural & Molecular Biology* **15**:1176–1183. DOI: https://doi.org/10.1038/nsmb.1476, PMID: 18953337

Fellmann C, Hoffmann T, Sridhar V, Hopfgartner B, Muhar M, Roth M, Lai DY, Barbosa IAM, Kwon JS, Guan Y, Sinha N, Zuber J. 2013. An optimized microrna backbone for effective single-copy rnai. *Cell Reports* **5**:1704–1713. DOI: https://doi.org/10.1016/j.celrep.2013.11.020, PMID: 24332856

Frank DB, Peng T, Zepp JA, Snitow M, Vincent TL, Penkala IJ, Cui Z, Herriges MJ, Morley MP, Zhou S, Lu MM, Morrisey EE. 2016. Emergence of a wave of wnt signaling that regulates lung alveologenesis by controlling epithelial self-renewal and differentiation. *Cell Reports* **17**:2312–2325. DOI: https://doi.org/10.1016/j.celrep.2016.11.001, PMID: 27880906

Habermann AC, Gutierrez AJ, Bui LT, Yahn SL, Winters NI, Calvi CL, Peter L, Chung M-I, Taylor CJ, Jetter C, Raju L, Roberson J, Ding G, Wood L, Sucre JMS, Richmond BW, Serezani AP, McDonnell WJ, Mallal SB, Bacchetta MJ, et al. 2020. Single-cell RNA sequencing reveals profibrotic roles of distinct epithelial and mesenchymal lineages in pulmonary fibrosis. *Science Advances* **6**:eaba1972. DOI: https://doi.org/10.1126/sciadv.aba1972, PMID: 32832598

Heinz S, Benner C, Spann N, Bertolino E, Lin YC, Laslo P, Cheng JX, Murre C, Singh H, Glass CK. 2010. Simple combinations of lineage-determining transcription factors prime cis-regulatory elements required for macrophage and B cell identities. *Molecular Cell* **38**:576–589. DOI: https://doi.org/10.1016/j.molcel.2010.05.004, PMID: 20513432

Hemberger M, Dean W, Reik W. 2009. Epigenetic dynamics of stem cells and cell lineage commitment: digging waddington's canal. *Nature Reviews. Molecular Cell Biology* **10**:526–537. DOI: https://doi.org/10.1038/nrm2727, PMID: 19603040

Huang T, Zhang P, Li W, Zhao T, Zhang Z, Chen S, Yang Y, Feng Y, Li F, Shirley Liu X, Zhang L, Jiang G, Zhang F. 2017. G9A promotes tumor cell growth and invasion by silencing CASP1 in non-small-cell lung cancer cells. *Cell Death & Disease* **8**:e2726. DOI: https://doi.org/10.1038/cddis.2017.65, PMID: 28383547

Huber W, Carey VJ, Gentleman R, Anders S, Carlson M, Carvalho BS, Bravo HC, Davis S, Gatto L, Girke T, Gottardo R, Hahne F, Hansen KD, Irizarry RA, Lawrence M, Love MI, MacDonald J, Obenchain V, Oleś AK, Pagès H, et al. 2015. Orchestrating high-throughput genomic analysis with bioconductor. *Nature Methods* **12**:115–121. DOI: https://doi.org/10.1038/nmeth.3252, PMID: 25633503

Jackson EL, Willis N, Mercer K, Bronson RT, Crowley D, Montoya R, Jacks T, Tuveson DA. 2001. Analysis of lung tumor initiation and progression using conditional expression of oncogenic K-ras. *Genes & Development* **15**:3243–3248. DOI: https://doi.org/10.1101/gad.943001, PMID: 11751630

Jonkers J, Meuwissen R, van der Gulden H, Peterse H, van der Valk M, Berns A. 2001. Synergistic tumor suppressor activity of BRCA2 and p53 in a conditional mouse model for breast cancer. *Nature Genetics* **29**:418–425. DOI: https://doi.org/10.1038/ng747, PMID: 11694875

Juan J, Muraguchi T, Iezza G, Sears RC, McMahon M. 2014. Diminished WNT -> β-catenin -> c-MYC signaling is a barrier for malignant progression of BRAFV600E-induced lung tumors. *Genes & Development* **28**:561–575. DOI: https://doi.org/10.1101/gad.233627.113, PMID: 24589553

Kim Y, Lee HM, Xiong Y, Sciaky N, Hulbert SW, Cao X, Everitt JI, Jin J, Roth BL, Jiang YH. 2017. Targeting the histone methyltransferase g9a activates imprinted genes and improves survival of a mouse model of prader-willi syndrome. *Nature Medicine* **23**:213–222. DOI: https://doi.org/10.1038/nm.4257, PMID: 28024084

Lee JS, Kim Y, Kim IS, Kim B, Choi HJ, Lee JM, Shin H-JR, Kim JH, Kim J-Y, Seo S-B, Lee H, Binda O, Gozani O, Semenza GL, Kim M, Kim KI, Hwang D, Baek SH. 2010. Negative regulation of hypoxic responses via induced reptin methylation. *Molecular Cell* **39**:71–85. DOI: https://doi.org/10.1016/j.molcel.2010.06.008, PMID: 20603076

Lee CL, Moding EJ, Huang X, Li Y, Woodlief LZ, Rodrigues RC, Ma Y, Kirsch DG. 2012. Generation of primary tumors with flp recombinase in FRT-flanked p53 mice. *Disease Models & Mechanisms* **5**:397–402. DOI: https://doi.org/10.1242/dmm.009084, PMID: 22228755

Lee J-H, Kim J, Gludish D, Roach RR, Saunders AH, Barrios J, Woo AJ, Chen H, Conner DA, Fujiwara Y, Stripp BR, Kim CF. 2013. Surfactant protein-C chromatin-bound green fluorescent protein reporter mice reveal heterogeneity of surfactant protein C-expressing lung cells. *American Journal of Respiratory Cell and Molecular Biology* **48**:288–298. DOI: https://doi.org/10.1165/rcmb.2011-0403OC, PMID: 23204392

Liberzon A, Birger C, Thorvaldsdóttir H, Ghandi M, Mesirov JP, Tamayo P. 2015. The molecular signatures database (msigdb) hallmark gene set collection. *Cell Systems* **1**:417–425. DOI: https://doi.org/10.1016/j.cels.2015.12.004, PMID: 26771021

Liu F, Barsyte-Lovejoy D, Li F, Xiong Y, Korboukh V, Huang X-P, Allali-Hassani A, Janzen WP, Roth BL, Frye SV, Arrowsmith CH, Brown PJ, Vedadi M, Jin J. 2013. Discovery of an in vivo chemical probe of the lysine methyltransferases g9a and GLP. *Journal of Medicinal Chemistry* **56**:8931–8942. DOI: https://doi.org/10.1021/jm401480r, PMID: 24102134

Madisen L, Zwingman TA, Sunkin SM, Oh SW, Zariwala HA, Gu H, Ng LL, Palmiter RD, Hawrylycz MJ, Jones AR, Lein ES, Zeng H. 2010. A robust and high-throughput cre reporting and characterization system for the whole mouse brain. *Nature Neuroscience* **13**:133–140. DOI: https://doi.org/10.1038/nn.2467, PMID: 20023653

Mainardi S, Mijimolle N, Francoz S, Vicente-Dueñas C, Sánchez-García I, Barbacid M. 2014. Identification of cancer initiating cells in K-ras driven lung adenocarcinoma. *PNAS* **111**:255–260. DOI: https://doi.org/10.1073/pnas.1320383110, PMID: 24367082

Mao YQ, Houry WA. 2017. The role of pontin and reptin in cellular physiology and cancer etiology. *Frontiers in Molecular Biosciences* **4**:58. DOI: https://doi.org/10.3389/fmolb.2017.00058, PMID: 28884116

McQualter JL, Yuen K, Williams B, Bertoncello I. 2010. Evidence of an epithelial stem/progenitor cell hierarchy in the adult mouse lung. *PNAS* **107**:1414–1419. DOI: https://doi.org/10.1073/pnas.0909207107, PMID: 20080639

Meerbrey KL, Hu G, Kessler JD, Roarty K, Li MZ, Fang JE, Herschkowitz JI, Burrows AE, Ciccia A, Sun T, Schmitt EM, Bernardi RJ, Fu X, Bland CS, Cooper TA, Schiff R, Rosen JM, Westbrook TF, Elledge SJ. 2011. The pinducer lentiviral toolkit for inducible RNA interference in vitro and in vivo. *PNAS* **108**:3665–3670. DOI: https://doi.org/10.1073/pnas.1019736108, PMID: 21307310

Nabhan AN, Brownfield DG, Harbury PB, Krasnow MA, Desai TJ. 2018. Single-cell wnt signaling niches maintain stemness of alveolar type 2 cells. Science **359**:1118–1123. DOI: https://doi.org/10.1126/science.aam6603, PMID: 29420258

Pacheco-Pinedo EC, Durham AC, Stewart KM, Goss AM, Lu MM, Demayo FJ, Morrisey EE. 2011. Wnt/β-catenin signaling accelerates mouse lung tumorigenesis by imposing an embryonic distal progenitor phenotype on lung epithelium. *The Journal of Clinical Investigation* **121**:1935–1945. DOI: https://doi.org/10.1172/JCI44871, PMID: 21490395

Pal A, Leung JY, Ang GCK, Rao VK, Pignata L, Lim HJ, Hebrard M, Chang KT, Lee VK, Guccione E, Taneja R. 2020. EHMT2 epigenetically suppresses wnt signaling and is a potential target in embryonal rhabdomyosarcoma. *eLife* **9**:e57683. DOI: https://doi.org/10.7554/eLife.57683, PMID: 33252038

Pau GB, Lawrence J, Degenhardt M, Wu J, Huntley T, Brauer MM. 2012. HTSeqGenie: a software package to analyse high-throughput sequencing experiments. Bioconductor. https://bioconductor.riken.jp/packages/2.14/bioc/html/HTSeqGenie.html

Pribluda A. 2020. G9a.cellidentity.lung. swh:1:rev:207a6bd1022c199eaae3ef0d2fcc9e4edcbb3c69. Software Heritage. https://archive.softwareheritage.org/swh:1:dir:7e1f0e1fd711899b8dfc98d98d8f5001b4bb9cde;origin=https://github.com/anneleendaemen/G9a.CellIdentity.Lung;visit=swh:1:snp:54991c3a34b735001fc036c8e0be7f28580cf11e;anchor=swh:1:rev:207a6bd1022c199eaae3ef0d2fcc9e4edcbb3c69

Reya T, Morrison SJ, Clarke MF, Weissman IL. 2001. Stem cells, cancer, and cancer stem cells. *Nature* **414**:105–111. DOI: https://doi.org/10.1038/35102167, PMID: 11689955

Robinson MD, Oshlack A. 2010. A scaling normalization method for differential expression analysis of RNA-seq data. *Genome Biology* **11**:R25. DOI: https://doi.org/10.1186/gb-2010-11-3-r25, PMID: 20196867

Robinson JT, Thorvaldsdóttir H, Winckler W, Guttman M, Lander ES, Getz G, Mesirov JP. 2011. Integrative genomics viewer. *Nature Biotechnology* **29**:24–26. DOI: https://doi.org/10.1038/nbt.1754, PMID: 21221095

Rowbotham SP, Li F, Dost AFM, Louie SM, Marsh BP, Pessina P, Anbarasu CR, Brainson CF, Tuminello SJ, Lieberman A, Ryeom S, Schlaeger TM, Aronow BJ, Watanabe H, Wong KK, Kim CF. 2018. H3K9 methyltransferases and demethylases control lung tumor-propagating cells and lung cancer progression. *Nature Communications* **9**:4559. DOI: https://doi.org/10.1038/s41467-018-07077-1, PMID: 30455465

Ruijtenberg S, van den Heuvel S. 2016. Coordinating cell proliferation and differentiation: antagonism between cell cycle regulators and cell type-specific gene expression. *Cell Cycle* **15**:196–212. DOI: https://doi.org/10.1080/15384101.2015.1120925, PMID: 26825227

Shackleton M, Quintana E, Fearon ER, Morrison SJ. 2009. Heterogeneity in cancer: cancer stem cells versus clonal evolution. *Cell* **138**:822–829. DOI: https://doi.org/10.1016/j.cell.2009.08.017, PMID: 19737509

Shechter D, Dormann HL, Allis CD, Hake SB. 2007. Extraction, purification and analysis of histones. *Nature Protocols* **2**:1445–1457. DOI: https://doi.org/10.1038/nprot.2007.202, PMID: 17545981

Shibata H, Komura S, Yamada Y, Sankoda N, Tanaka A, Ukai T, Kabata M, Sakurai S, Kuze B, Woltjen K, Haga H, Ito Y, Kawaguchi Y, Yamamoto T, Yamada Y. 2018. In vivo reprogramming drives kras-induced cancer development. *Nature Communications* **9**:2081. DOI: https://doi.org/10.1038/s41467-018-04449-5, PMID: 29802314

Shinkai Y, Tachibana M. 2011. H3K9 methyltransferase g9a and the related molecule GLP. *Genes & Development* **25**:781–788. DOI: https://doi.org/10.1101/gad.2027411, PMID: 21498567

Sutherland KD, Song JY, Kwon MC, Proost N, Zevenhoven J, Berns A. 2014. Multiple cells-of-origin of mutant K-ras-induced mouse lung adenocarcinoma. *PNAS* **111**:4952–4957. DOI: https://doi.org/10.1073/pnas.1319963111, PMID: 24586047

Tammela T, Sanchez-Rivera FJ, Cetinbas NM, Wu K, Joshi NS, Helenius K, Park Y, Azimi R, Kerper NR, Wesselhoeft RA, Gu X, Schmidt L, Cornwall-Brady M, Yilmaz ÖH, Xue W, Katajisto P, Bhutkar A, Jacks T. 2017. A wnt-producing niche drives proliferative potential and progression in lung adenocarcinoma. *Nature* **545**:355–359. DOI: https://doi.org/10.1038/nature22334, PMID: 28489818

Treutlein B, Brownfield DG, Wu AR, Neff NF, Mantalas GL, Espinoza FH, Desai TJ, Krasnow MA, Quake SR. 2014. Reconstructing lineage hierarchies of the distal lung epithelium using single-cell RNA-seq. *Nature* **509**:371–375. DOI: https://doi.org/10.1038/nature13173, PMID: 24739965

Widschwendter M, Fiegl H, Egle D, Mueller-Holzner E, Spizzo G, Marth C, Weisenberger DJ, Campan M, Young J, Jacobs I, Laird PW. 2007. Epigenetic stem cell signature in cancer. *Nature Genetics* **39**:157–158. DOI: https://doi.org/10.1038/ng1941, PMID: 17200673

Wu TD, Nacu S. 2010. Fast and SNP-tolerant detection of complex variants and splicing in short reads. *Bioinformatics* **26**:873–881. DOI: https://doi.org/10.1093/bioinformatics/btq057, PMID: 20147302

Xu X, Rock JR, Lu Y, Futtner C, Schwab B, Guinney J, Hogan BLM, Onaitis MW. 2012. Evidence for type II cells as cells of origin of K-ras-induced distal lung adenocarcinoma. *PNAS* **109**:4910–4915. DOI: https://doi.org/10.1073/pnas.1112499109, PMID: 22411819

Zacharias WJ, Frank DB, Zepp JA, Morley MP, Alkhaleel FA, Kong J, Zhou S, Cantu E, Morrisey EE. 2018. Regeneration of the lung alveolus by an evolutionarily conserved epithelial progenitor. *Nature* **555**:251–255. DOI: https://doi.org/10.1038/nature25786, PMID: 29489752

Zepp JA, Zacharias WJ, Frank DB, Cavanaugh CA, Zhou S, Morley MP, Morrisey EE. 2017. Distinct mesenchymal lineages and niches promote epithelial self-renewal and myofibrogenesis in the lung. *Cell* **170**:1134–1148. DOI: https://doi.org/10.1016/j.cell.2017.07.034, PMID: 28886382

Zhang Y, Liu T, Meyer CA, Eeckhoute J, Johnson DS, Bernstein BE, Nusbaum C, Myers RM, Brown M, Li W, Liu XS. 2008. Model-based analysis of chip-seq (macs). *Genome Biology* **9**:R137. DOI: https://doi.org/10.1186/gb-2008-9-9-r137, PMID: 18798982

Zhang K, Wang J, Yang L, Yuan Y-C, Tong TR, Wu J, Yun X, Bonner M, Pangeni R, Liu Z, Yuchi T, Kim JY, Raz DJ. 2018. Targeting histone methyltransferase g9a inhibits growth and wnt signaling pathway by epigenetically regulating hp1α and APC2 gene expression in non-small cell lung cancer. *Molecular Cancer* **17**:153. DOI: https://doi.org/10.1186/s12943-018-0896-8, PMID: 30348169

Zheng Y, de la Cruz CC, Sayles LC, Alleyne-Chin C, Vaka D, Knaak TD, Bigos M, Xu Y, Hoang CD, Shrager JB, Fehling HJ, French D, Forrest W, Jiang Z, Carano RAD, Barck KH, Jackson EL, Sweet-Cordero EA. 2013. A rare population of CD24(+)ITGB4(+)notch(hi) cells drives tumor propagation in NSCLC and requires notch3 for self-renewal. *Cancer Cell* **24**:59–74. DOI: https://doi.org/10.1016/j.ccr.2013.05.021, PMID: 23845442

Zylicz JJ, Borensztein M, Wong FC, Huang Y, Lee C, Dietmann S, Surani MA. 2018. G9a regulates temporal preimplantation developmental program and lineage segregation in blastocyst. *eLife* **7**:e33361. DOI: https://doi.org/10.7554/eLife.33361, PMID: 29745895